

# Can three-flavor oscillations solve the solar neutrino problem?

H. Schlattl\*

Max-Planck-Institut für Astrophysik, Karl-Schwarzschild-Str. 1, 85741 Garching, Germany

(December 6, 2018)

The good agreement of standard solar models with helioseismology and the combined analysis of the solar neutrino experiments suggest that the solution to the solar neutrino problem is located in particle physics rather than in astrophysics. The most promising solution are neutrino oscillations, which usually are analyzed within the reduced 2-flavor scheme, because the solutions found therein reasonably well reproduce the recent data of Super-Kamiokande about the recoil-electron energy spectrum, zenith-angle and seasonal variations, and the event rate data of all the neutrino detectors. In this work, however, a survey of the complete parameter space of 3-flavor oscillations is performed. Basically eight new additional solutions could be identified, where the best one with  $\Delta m_{12}^2 = 2.7 \times 10^{-10} \text{ eV}^2$ ,  $\Delta m_{13}^2 = 1.0 \times 10^{-5} \text{ eV}^2$ ,  $\Theta_{12} = 23^\circ$ , and  $\Theta_{13} = 1.3^\circ$  (denoted SVO) is slightly more probable than any 2-flavor solution. While the 2-flavor results of the atmospheric neutrino problem ( $\Delta m_{23}^2 \gtrsim 10^{-3} \text{ eV}^2$ ) would exclude all the 3-flavor solutions of this work, in the 3-flavor atmospheric-neutrino analysis the SLMA-solution with  $\Delta m_{12}^2 = 7.9 \times 10^{-6} \text{ eV}^2$ ,  $\Delta m_{13}^2 = 2.5 \times 10^{-4} \text{ eV}^2$ ,  $\Theta_{12} = 1.4^\circ$ , and  $\Theta_{13} = 20^\circ$  is still allowed. The relatively weak improvement of the fit using 3-flavor instead of 2-flavor oscillations, which appears to be due to an inconsistency of the different kind of data, indicates that there are possibly still systematic errors in at least one data set, or that the statistics is not yet sufficient. Besides, the ability of SNO and Borexino to discriminate the various 2- and 3-flavor solutions is investigated. Only with very good statistics in these experiments the correct solution to the solar neutrino problem can be identified unambiguously.

PACS numbers: 26.65.+t, 14.60.Pq, 96.60.Jw

## I. INTRODUCTION

From the beginning of the first measurements of the solar neutrino flux on Earth [1] until the present time, the origin of the solar neutrino problem could not yet be resolved totally. While previously inaccurate or unknown physics used in solar-model calculations could have been made responsible for the discrepancy between measured and predicted solar neutrino flux, this kind of solution can presently almost be ruled out, basically of two reasons:

Firstly, the high precision in the measurements of the solar p-mode frequencies and the development of helioseismological inversion techniques enable the determination of the solar sound-speed profile with high accuracy [2]. The comparison with standard solar models containing improved input physics like opacity, equation of state and microscopic diffusion shows an excellent agreement with the seismic models [3–5]. Predictions for the event rates in the solar neutrino detectors deduced from these standard solar models still are inconsistent with the measurements, confirming the solar neutrino problem (Table II).

Secondly, the three types of currently operating experiments, the chlorine detector [1], the gallium experiments GALLEX/GNO [6] and SAGE [7], and the Čerenkov-light counter Super-Kamiokande have different neutrino-

energy thresholds. This allows to determine the contribution of different parts of the solar neutrino spectrum to the total flux without explicitly taking into account solar-model calculations. From this analysis it has been inferred that the experimental results can be explained only with huge changes in the nuclear fusion rates. The best fit with the data is obtained even with a *negative* flux of neutrinos created in the electron-capture process of  ${}^7\text{Be}$  [8]. Nevertheless, strong modifications of the reaction cross sections would be difficult to explain experimentally and theoretically. Moreover, even if a presently unknown physical process can account for the demanded changes, the resulting solar models would hardly be consistent with helioseismology [9].

The most promising approach to the solution of the solar neutrino problem is an extension to the particle-physics standard model — neutrino mixing. Analogous to the CKM-mixing in the quark sector, weak and mass eigenstates of the neutrinos are supposed not to be identical but connected by a unitary transformation.

Under this assumption an initial solar electron-neutrino can be converted during its propagation to the Earth into another flavor, a  $\mu$ - or  $\tau$ -neutrino (*just-so* oscillations [10]). Furthermore, the neutrinos may coherently scatter forward in solar matter (*MSW-effect* [11]) altering the conversion probability for a certain set of mixing parameters.

The possible values for the mixing parameters, with which the measured event rates in all detectors can be reproduced simultaneously, have been derived by various authors [12,13], but only the oscillations between two flavors usually is taken into account.

---

\*e-mail address: schlattl@mpa-garching.mpg.de

Recently Super-Kamiokande has published more detailed information about the energy distribution of the recoiled electrons and the zenith-angle dependence of the neutrino-signal [14,15]. In the analysis of the 825-days data it became clear, that it is not possible to explain satisfactorily these data *and* the event rates of all detectors by one set of mixing parameters (see [16]): An excess of event rates in the high-energy bins was inconsistent with the other data.

It was the initial motivation of the present work to examine, whether an expansion of the neutrino analysis to the more general 3-flavor case could resolve this discrepancy between the different types of data. However, after the Super-Kamiokande group reanalyzed their data and included new data (1117 days in total), in particular the excess in the energy-bin data could be diminished and now all kind of data can be explained simultaneously by 2-flavor oscillations. Furthermore, the neutrino spectrum in the  $^8\text{B}$ -decay has been measured recently in the laboratory [17]. Although within the errors the spectrum is in agreement with the one predicted theoretically in [18], the number of high-energetic neutrinos is overall higher than previously thought. Thus, the excess in the high-energy bins is further reduced which yields a yet slightly better reproduction of the data by the 2-flavor solutions (see section IV A). Nevertheless, it is presently still not clear, which solution to the solar neutrino problem is the correct one, and hence all possible solution should be deduced.

Therefore, in this work the most general case of 3-flavor oscillations is investigated without making any assumptions about the mass scale as, for instance, inspired by the atmospheric neutrino problem. The latter is taken in various publications [20–22] as a constraint to investigate 3-flavor oscillations. But here, the aim is to examine whether the expansion to three flavors leads to new solutions with which the fits to all kind of data can be improved compared to the usual 2-flavor analysis. The implications for the atmospheric neutrino puzzle are discussed afterwards.

In section II the equations for 3-flavor oscillations are derived from the solution to the Klein-Gordon equation and the size of the parameter space is deduced. After describing the underlying solar model and the neutrino analysis in section III, the results for 2-flavor and 3-flavor oscillations are shown (section IV). Finally the ability of forthcoming experiments like SNO and Borexino to discriminate the various solutions are discussed (section V).

## II. THEORY OF NEUTRINO OSCILLATIONS

In the following an overview of the basic equations for neutrino oscillations are provided with particular emphasis to the 3-flavor case. A more thorough description can be found e.g. in [23] or [9].

### A. Vacuum oscillations

If neutrinos have mass, a mixing matrix similar to the Kobayashi-Maskawa matrix in the quark sector can be developed

$$|\nu_\alpha\rangle = \begin{pmatrix} \nu_e \\ \nu_\mu \\ \nu_\tau \end{pmatrix} = \mathcal{U} \begin{pmatrix} \nu_1 \\ \nu_2 \\ \nu_3 \end{pmatrix} = \mathcal{U} |\nu_i\rangle, \quad (1)$$

where  $|\nu_\alpha\rangle$  denotes the weak and  $|\nu_i\rangle$  the mass eigenstates. The unitary matrix  $\mathcal{U}$  can be parameterized by

$$\mathcal{U} = \begin{pmatrix} 1 & 0 & 0 \\ 0 & c_{23} & s_{23} \\ 0 & -s_{23} & c_{23} \end{pmatrix} \begin{pmatrix} c_{13} & 0 & s_{13}e^{-i\delta} \\ 0 & 1 & 0 \\ -s_{13}e^{i\delta} & 0 & c_{13} \end{pmatrix} \times \begin{pmatrix} c_{12} & s_{12} & 0 \\ -s_{12} & c_{12} & 0 \\ 0 & 0 & 1 \end{pmatrix} \quad (2)$$

where  $s_{ij}$  and  $c_{ij}$  are abbreviations for  $\sin \Theta_{ij}$  resp.  $\cos \Theta_{ij}$  ( $0 \leq \Theta_{ij} < \pi/2$ ) and  $\delta$  is a CP-violating phase [24], which is neglected in the following<sup>†</sup>. The equation of motion for a neutrino beam in vacuum obeys the Klein-Gordon equation for free particles ( $\hbar = c = 1$ )

$$(\partial_t^2 - \nabla^2 + M^2) |\nu_i(t, \vec{r})\rangle = 0, \quad (3)$$

where the mass matrix  $M^2$  is defined as

$$M^2 = \begin{pmatrix} m_1^2 & 0 & 0 \\ 0 & m_2^2 & 0 \\ 0 & 0 & m_3^2 \end{pmatrix}$$

with  $m_i$  being the mass of the neutrino mass eigenstate  $\nu_i$ . Generally the solution is given by a superposition of plane waves  $e^{i(\vec{k}\vec{r} - \omega t)}$  with the dispersion relation

$$\omega^2 = \vec{k}^2 + m^2.$$

In the case of the Sun with an almost stationary neutrino flux,  $|\nu_i(t, \vec{r})\rangle$  can be expanded in components of fixed frequency  $|\nu_i(\vec{r})\rangle_\omega e^{-i\omega t}$ . For a spherically symmetric flux of relativistic neutrinos ( $k \approx \omega$ ) one finally gets

$$-i \frac{\partial}{\partial r} |\nu_i(r)\rangle_\omega = \left( \omega - \frac{M^2}{2\omega} \right) |\nu_i(r)\rangle_\omega. \quad (4)$$

The constant ‘‘potential’’  $\omega$  can be removed by shifting the energy scale, and by using  $t = r$  Eq. (4) can be formally written as a more familiar Schrödinger-type equation

$$i \frac{\partial}{\partial t} |\nu_i(t)\rangle_\omega = \mathcal{H} |\nu_i(t)\rangle_\omega \quad (5)$$

---

<sup>†</sup>The effect of the CP-violating phase on the analysis of neutrino oscillation data has been elaborated in [25]

with  $\mathcal{H} = E_{\text{kin}} \approx \frac{M^2}{2\omega}$ . The general solution to this equation is

$$|\nu_i(t)\rangle_\omega = e^{-it\frac{M^2}{2\omega}} |\nu_i(t_0)\rangle_\omega. \quad (6)$$

The probability  $P(r)_{\alpha\rightarrow\beta}$  to detect a neutrino  $\nu_\alpha$  with energy  $E = \omega$  as a neutrino of type  $\nu_\beta$  at distance  $r = t$  from the source is therefore given by ( $\mathcal{U}^{-1} = \mathcal{U}^\dagger$ )

$$P(r)_{\alpha\rightarrow\beta} = \left| \langle \nu_\beta | \mathcal{U} e^{-ir\left(\frac{\Delta M^2}{2E}\right)} \mathcal{U}^\dagger | \nu_\alpha \rangle \right|^2. \quad (7)$$

Using  $\Delta m_{ij}^2 = m_j^2 - m_i^2$  the matrix  $\Delta M^2$  writes as

$$\Delta M^2 = M^2 - m_1^2 Id_3 = \begin{pmatrix} 0 & 0 & 0 \\ 0 & \Delta m_{12}^2 & 0 \\ 0 & 0 & \Delta m_{13}^2 \end{pmatrix}.$$

With the mass eigenstate of an electron-neutrino being

$$\begin{pmatrix} \nu_1 \\ \nu_2 \\ \nu_3 \end{pmatrix}_e = \mathcal{U}^\dagger \begin{pmatrix} 1 \\ 0 \\ 0 \end{pmatrix} = \begin{pmatrix} c_{12}c_{13} \\ s_{12}c_{13} \\ s_{13} \end{pmatrix}, \quad (8)$$

Eq. (7) yields for the survival probability of  $\nu_e$ 's in vacuum

$$\begin{aligned} P(r)_{e\rightarrow e}^{(3)} &= 1 - \sin^2\left(\frac{\Delta m_{12}^2 r}{4E}\right) \cos^4\Theta_{13} \sin^2 2\Theta_{12} \\ &\quad - \left[ \sin^2\left(\frac{\Delta m_{13}^2 r}{4E}\right) \cos^2\Theta_{12} \right. \\ &\quad \left. + \sin^2\left(\frac{\Delta m_{23}^2 r}{4E}\right) \sin^2\Theta_{12} \right] \sin^2 2\Theta_{13}. \end{aligned} \quad (9)$$

The superscript (3) denotes the case of 3-flavor mixing.  $P_{e\rightarrow e}^{(3)}$  depends on four quantities, two mass-squared differences,  $\Delta m_{12}^2$  and  $\Delta m_{13}^2$  ( $\Delta m_{23}^2 = \Delta m_{13}^2 - \Delta m_{12}^2$ ), and two mixing angles  $\Theta_{12}$  and  $\Theta_{13}$ . The third mixing angle  $\Theta_{23}$  does not appear in Eq. (8) and hence  $P_{e\rightarrow e}^{(3)}$  is independent of this quantity. The survival probabilities for  $\nu_\mu$  and  $\nu_\tau$  depend on  $\Theta_{23}$ , but its value cannot be determined by solar-neutrino experiments, as in the energy range of the solar neutrinos  $\nu_\mu$  and  $\nu_\tau$  interact equally with the detector material via NC-interactions. Thus, only the total number of  $\mu$ - plus  $\tau$ -neutrinos, given by  $1 - P_{e\rightarrow e}^{(3)}$ , influences the event rates in detectors like Super-Kamiokande, SNO or Borexino.

For oscillations between two neutrino flavors where no mixing into the third flavor occurs (e.g.  $\nu_e \leftrightarrow \nu_\mu$ ,  $\Theta_{13} = 0$ ), Eq. (9) simplifies to the well known formula

$$P(r)_{e\rightarrow e}^{(2)} = 1 - \sin^2\left(\frac{\Delta m^2 r}{4E}\right) \sin^2 2\Theta, \quad (10)$$

where  $\Delta m^2 = \Delta m_{12}^2$  or  $\Delta m_{13}^2$  for  $\nu_e$ - $\nu_\mu$ - resp.  $\nu_e$ - $\nu_\tau$ -oscillations ( $\Theta$  defined analogously).

## B. Matter effect

During the propagation of the neutrinos through the Sun they coherently scatter forward on the particles of the solar plasma. Unlike  $\mu$ - and  $\tau$ -neutrinos, which only interact via NC-reactions, electron-neutrinos can additionally couple via  $\mathcal{W}$ -bosons to the electrons. Thus, the scattering cross section of a  $\nu_e$  is altered as against the one of the other two neutrino-flavors. This can lead to a resonant flavor transition, which may create a pure  $\nu_\mu$ - or  $\nu_\tau$ -beam from the originally created electron-neutrinos, first theoretically postulated and described in [11] (*MSW-effect*).

This effect can be included in Eq. (5) by substituting  $\mathcal{H}$  with  $\tilde{\mathcal{H}} = \mathcal{H} + V_{\text{eff}}$ , where

$$V_{\text{eff}} = \sqrt{2} G_F N_e \mathcal{U}^\dagger \begin{pmatrix} 1 & 0 & 0 \\ 0 & 0 & 0 \\ 0 & 0 & 0 \end{pmatrix} \mathcal{U}$$

influences solely the  $\nu_e$ -contribution of the neutrino beam.  $G_F$  is the Fermi coupling-constant and  $N_e$  the electron number density. The new Hamiltonian  $\tilde{\mathcal{H}}$  is no longer diagonal in the mass basis. To evaluate the survival probability and thus  $\exp(-i\tilde{\mathcal{H}}t)$  it is therefore necessary to diagonalize  $\tilde{\mathcal{H}}$  by a unitary transformation  $\mathcal{V}$

$$\tilde{\mathcal{H}}_m = \begin{pmatrix} M_1 & 0 & 0 \\ 0 & M_2 & 0 \\ 0 & 0 & M_3 \end{pmatrix} = \mathcal{V}^\dagger \tilde{\mathcal{H}} \mathcal{V}.$$

Similar to the vacuum oscillations the constant phase  $M_1 Id_3$  can be removed from  $\tilde{\mathcal{H}}$  as it does not change the survival probability. The complicated analytical expressions for  $\Delta M_{ij}$  have been evaluated in [26]. Recently,  $\exp(-i\tilde{\mathcal{H}}t)$  has been calculated in [27] by using Cayley-Hamilton's theorem without explicitly deriving  $\mathcal{V}$ . In the present work, however,  $\mathcal{V}$  and  $M_i$  are computed with a fast numerical algorithm using none of the analytic expressions.

## C. The parameter space

Recently various publications came up about the actual size of the necessary parameter space covering all possible solutions of the solar neutrino problem [28–30]. In this section the sometimes confusing statements about this topic are summarized and clarified.

The mixing angles can be defined to lie in the first quadrant by appropriately adjusting the neutrino field phases similar as in the quark sector [31]. This can also be verified from the final formulae, as, for instance,  $P(r)_{e\rightarrow e}^{(3)}$  depends solely on the square of  $\sin\Theta_{ij}$  resp.  $\cos\Theta_{ij}$  ( $ij = 12, 13$ ). Moreover, it has been shown in [28] that it is also sufficient to consider  $0 \leq \Theta_{23} < \pi/2$ , if  $P(r)_{e\rightarrow\mu}^{(3)}$  resp.  $P(r)_{e\rightarrow\tau}^{(3)}$  are to be measured. In the case of the

matter-enhanced oscillations the situation is not as trivial, but using an analytical formula for the evolution of a neutrino state in matter as derived in [27] (Eq. 44 therein), one can also show that the evolution of an initial electron-neutrino is determined only by the squares of  $\sin \Theta_{ij}$  and  $\cos \Theta_{ij}$ .

### 1. Two flavors

First, the case of 2-flavor oscillations is examined. Exchanging the first and second row in the definition of the mass eigenstates (Eq. 1) implies that  $\Delta m^2 \rightarrow -\Delta m^2$  and  $\sin \Theta \leftrightarrow \cos \Theta$  ( $\Leftrightarrow \Theta \rightarrow (\pi/2 - \Theta)$ )<sup>‡</sup>. Since the assignment of the masses  $m_i$  to the respective mass eigenstate  $\nu_j$  must not change the results, e.g. the case  $\Delta m^2 > 0$ ,  $0 \leq \Theta < \pi/4$  is equivalent to  $\Delta m^2 < 0$ ,  $\pi/4 \leq \Theta < \pi/2$  for any possible form of the Hamiltonian. Thus, without loss of generality  $\Theta$  can be chosen to be within  $[0, \pi/4]$ .

For pure vacuum oscillations Eq. (10) can be applied which yields that  $P(r)_{e \rightarrow e}^{(2)}$  is independent of the sign of  $\Delta m^2$  and under the transformation  $\Theta \rightarrow (\pi/2 - \Theta)$ . Hence, in this case it is even sufficient to consider  $\Delta m^2 > 0$ .

The situation is different for oscillations in matter, where the resonance condition for MSW-transition is given by

$$N_{\text{res}} = \frac{\Delta m^2 / 2E}{\sqrt{2}G_{\text{F}}} \cos 2\Theta. \quad (11)$$

A resonance may occur, if  $N_{\text{res}}$  is positive, thus  $\Delta m^2 > 0$  ( $\Theta \leq \pi/4$ ). Although no resonance occurs for negative values of  $\Delta m^2$ , the matter still influences the evolution of the neutrino flavor composition in the solar interior (for a more detailed study see e.g. [26]).

In Fig. 1 the effect of solar matter on the energy dependence of  $P_{e \rightarrow e}^{(2)}$  is demonstrated. For  $E/|\Delta m^2| \lesssim 10^8 \text{ MeV/eV}^2$  vacuum oscillations would yield an energy-independent survival probability for electron-neutrinos, as the vacuum oscillation length is small and therefore only a mean value of (Eq. 10)

$$\langle P_{e \rightarrow e}^{(2)} \rangle_r = 1 - 0.5 \sin^2 2\Theta \quad (12)$$

would be measurable on Earth. For  $\sin^2 2\Theta = 0.7$  this leads to  $\langle P_{e \rightarrow e}^{(2)} \rangle_r = 0.65$ . In contrast to the case with  $\Delta m^2 > 0$  (solid line), where the resonant flavor conversion diminishes the  $\nu_e$ -contribution of the solar neutrino current, for  $\Delta m^2 < 0$  (dashed line) the  $\nu_e$ -portion is even enhanced compared to the pure vacuum-oscillation case. Thus, the minimum value of the  $\nu_e$ -contribution for

<sup>‡</sup>The indices 12 or 13 of the mass-squared difference resp. mixing angle are omitted in the 2-flavor case.

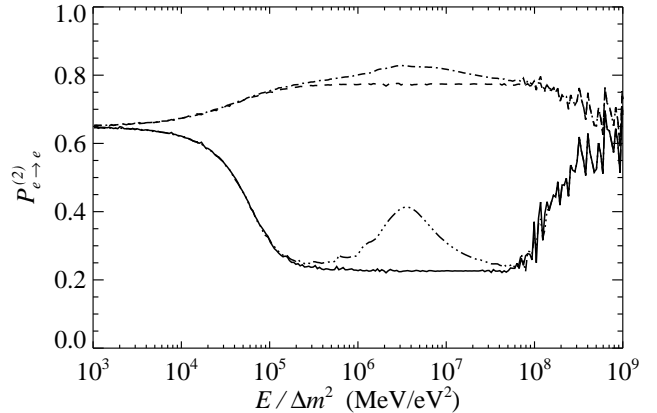


FIG. 1. Annually averaged probability of detecting a neutrino produced in the solar center as  $\nu_e$  on Earth for  $\sin^2 2\Theta = 0.7$  ( $0 \leq \Theta < \pi/4$ ) with  $\Delta m^2 > 0$  (solid and dash-dot-dot-dotted) resp.  $\Delta m^2 < 0$  (dashed and dash-dotted line). The two lines in each case show the probability neglecting (solid and dashed) resp. including (dash-dot-dot-dotted and dash-dotted) the Earth regeneration effect [33].

$\Delta m^2 < 0$  is obtained for pure vacuum oscillations. However, since vacuum oscillations in this mass range yield at most a suppression of the  $\nu_e$ -flux of 50% (Eq. 12) and the solution to the solar neutrino problem demands, at least to explain the Homestake experiment, a stronger suppression of about 60%, for  $\Delta m^2 < 0$  no reasonable solution can be obtained. Hence it is sufficient to consider in the 2-flavor MSW case similar to the 2-flavor vacuum oscillations solely  $\Delta m^2 > 0$  ( $\Theta \leq \pi/4$ ).

Recently, it has been pointed out in [30,32] that the  $3\sigma$ -ranges of the LMA- and LOW-solutions (see below) extend outside this region, but additional solutions for the solar neutrino problems cannot be found there. In their analysis, however,  $\Delta m^2$  was fixed to be positive and thus  $0 \leq \Theta < \pi/2$  has been examined. The region  $\pi/4 < \Theta < \pi/2$  of their parameter space (termed “the dark side”) is equivalent to the region  $\Delta m^2 < 0$  and  $0 \leq \Theta < \pi/4$  discussed above.

### 2. Three flavors

The considerations of the 2-flavor case are now extended to three flavors. In Fig. 2 the flavor space for the electron-neutrino is illustrated, where  $\nu_e$  is represented as a (yet unknown) point on the surface of an eight of a unit sphere. While in the 2-flavor case the ordering of the masses enables two cases to be distinguished ( $\Delta m^2 < 0$  resp.  $\Delta m^2 > 0$ ), in the 3-flavor scenario six cases can be identified. But, since exchanging any axes in Fig. 2 maps the flavor space onto itself, each mass hierarchy can of course be obtained from the “canonical” one ( $m_1^2 < m_2^2 < m_3^2$ ) simply by exchanging the respective assignment of  $m_i$  to  $\nu_j$  in Eq. (1).

Unlike the 2-flavor case, where for pure vacuum oscillations the parameter space could be further decreased, it is not possible in the general 3-flavor scenario, as e.g.  $\Delta m_{23}^2 = \Delta m_{13}^2 - \Delta m_{12}^2$ , is not invariant under the transformation  $\Delta m_{12}^2 \rightarrow -\Delta m_{12}^2$ .

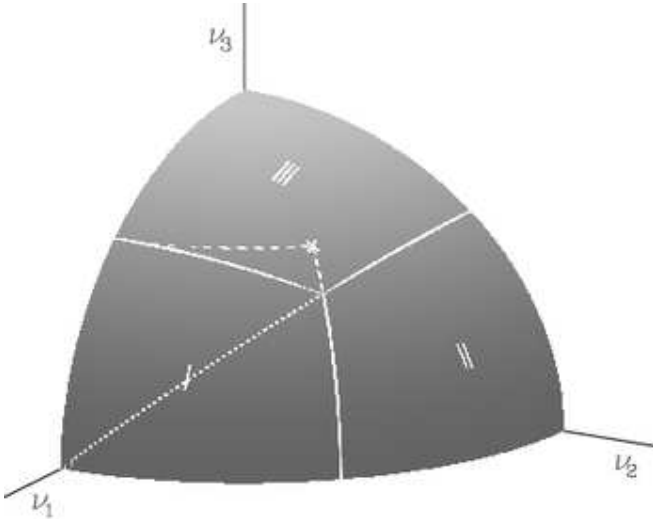


FIG. 2. Geometrical illustration of the flavor space available for a  $\nu_e$  in the mass basis  $(\nu_1, \nu_2, \nu_3)^T$ . The spherical segment is divided into three sectors of equal size and shape, where each can be obtained from another by mirroring at the respective diagonal. Maximal mixing is given at the intersection of all three sector borders, i.e.  $\sin^2 2\Theta_{12} = 1$  and  $\sin^2 2\Theta_{13} = \frac{8}{9}$ . The cross in sector III indicates the case  $\sin^2 2\Theta_{12} = \sin^2 2\Theta_{13} = 1$ , the dashed border extends sector I to the area with  $\Theta_{12}, \Theta_{13} \leq \pi/4$ . The dotted line splits sector I into two symmetric parts. (See text for more details.)

For 3-flavor neutrino oscillations in matter an exact analytic resonance condition can hardly be obtained because of the complicated formula for the mass eigenvalues  $\Delta M_{ij}$ . If the masses are well separated, the 2-flavor resonance condition (Eq. 11) can be applied for both systems by substituting the quantities  $(\Delta m_{12}^2, \cos 2\Theta)$  by  $(\Delta m_{12}^2 \cos \Theta_{13}, \cos 2\Theta_{12})$  resp.  $(\Delta m_{13}^2, \cos 2\Theta_{13})$  [34]. Hence, in this case considering  $\Theta_{12}, \Theta_{13} \leq \pi/4$  (sector I) extended to the dashed borders in sector III of Fig. 2) with  $\Delta m_{12}^2, \Delta m_{13}^2 \geq 0$  is sufficient to obtain all possible solutions where two resonances may occur. However, the solution to the solar neutrino problem may also be a combination of a non-resonant and a resonant oscillation and the masses can be in principle very similar, too. Thus, the whole parameter space must be taken into account.

In [20], for instance, 3-flavor oscillations were investigated assuming canonical mass hierarchy and using a fixed value for  $\Delta m_{13}^2 = 10^{-3} \text{ eV}^2$  in agreement with the atmospheric-neutrino results. They examined the remaining parameter space applying an analytical formula for the  $\nu_e$  survival probability, which approximates the solar electron-density profile by an exponential function

and is valid for  $\Delta m_{13}^2 \approx 10^{-3} \text{ eV}^2$  and  $\Delta m_{12}^2$  significantly smaller than  $\Delta m_{13}^2$ . Under these conditions the parameter space could be reduced considerably.

In the present work, the most general case of 3-flavor oscillations of solar neutrinos is investigated, and thus these restrictions are not applicable here. Instead of performing a survey over the whole flavor space ( $0 \leq \Theta_{12}, \Theta_{13} < \pi/2$ ) with canonical mass hierarchy, I prefer to consider the case  $\Delta m_{12}^2, \Delta m_{13}^2 > 0$  which covers two possible mass hierarchies. Thus, in this case only half of the total flavor space must be overviewed. In the illustration provided in Fig. 2 this reduced area is given by sector II and the lower half of sector I defined by the dotted line.

To simplify the numerical survey and the analysis a variable transformation to the mixing angles is applied in each sector: Obviously  $P_{e \rightarrow e}^{(3)}$  as defined in Eq. (9) is not symmetric under the exchange of the indices  $2 \leftrightarrow 3$ . However, sector I is symmetric under  $\nu_2 \leftrightarrow \nu_3$ , and it would be useful to have two quantities  $\tilde{\Theta}_{12}(\Theta_{12}, \Theta_{13})$  and  $\tilde{\Theta}_{13}(\Theta_{12}, \Theta_{13})$  which fulfill

$$P_{e \rightarrow e}^{(3)}(\Delta m_{12}^2, \tilde{\Theta}_{12}, \Delta m_{13}^2, \tilde{\Theta}_{13}) = P_{e \rightarrow e}^{(3)}(\Delta m_{13}^2, \tilde{\Theta}_{13}, \Delta m_{12}^2, \tilde{\Theta}_{12}).$$

Defining in sector I ( $0 \leq \Theta_{12} < \pi/4, \tan \Theta_{13} \leq \cos \Theta_{12}$ ) the quantities  $\tilde{s}_{12}(= \sin \tilde{\Theta}_{12})$  and  $\tilde{s}_{13}$  by

$$\begin{aligned} \tilde{s}_{12} &= s_{12} \\ \tilde{s}_{13} &= \frac{s_{13}}{\sqrt{1 - s_{12}^2 c_{13}^2}}, \end{aligned} \quad (13)$$

yields such a pair. With these quantities Eq. (9) writes as ( $\tilde{c}_{ij}^2 = 1 - \tilde{s}_{ij}^2$ )

$$P(r)_{e \rightarrow e}^{(3)} = 1 - \left( \frac{2\tilde{c}_{12}\tilde{c}_{13}}{1 - \tilde{s}_{12}^2\tilde{s}_{13}^2} \right)^2 \left[ \tilde{s}_{12}^2\tilde{c}_{13}^2 \sin^2 \left( \frac{\Delta m_{12}^2 r}{4E} \right) + \tilde{c}_{12}^2\tilde{s}_{13}^2 \sin^2 \left( \frac{\Delta m_{13}^2 r}{4E} \right) + \tilde{s}_{12}^2\tilde{s}_{13}^2 \sin^2 \left( \frac{\Delta m_{23}^2 r}{4E} \right) \right],$$

which is unaltered under the exchange of the indices  $2 \leftrightarrow 3$ .

Moreover, it can be proven that the evolution matrix of neutrinos in matter is not changed when exchanging the indices  $2 \leftrightarrow 3$  [9]. Hence, using  $\tilde{s}_{12}$  and  $\tilde{s}_{13}$  in sector I yields a  $\nu_e$  survival probability, which is constant under this transformation in vacuum as well as in matter.

Similar to sector I also sector II ( $\pi/4 \leq \Theta_{12} < \pi/2, \tan \Theta_{13} \leq \sin \Theta_{12}$ ) can be brought in a quadratic shape by using the transformation

$$\tilde{s}_{13} = \frac{s_{13}}{\sqrt{1 - c_{12}^2 c_{13}^2}}. \quad (14)$$

But this does not yield a survival probability invariant under the exchange of the indices  $2 \leftrightarrow 3$ , as under this operation sector II would be mapped on sector III.

### III. CALCULATIONS

#### A. Standard solar model

For the following calculations my standard solar model (“GARSOM4”) as described in [35] is used. It has been calculated using the latest input physics, equation of state and opacity from the OPAL-group [36,37], and nuclear reaction rates as proposed by [38]. In addition, microscopic diffusion of H,  $^3\text{He}$ ,  $^4\text{He}$ , the CNO-isotopes, and 4 heavier elements (among them Fe) is included using the diffusion constants of [39]. By treating convection as a fast diffusive process the chemical changes due to nuclear burning and diffusion (mixing) are evaluated in a common scheme.

A peculiarity of GARSOM4 is the inclusion of realistic 2d-hydrodynamical model atmospheres [40] until an optical depth of 1000. The improvement of the high-degree p-mode frequencies due to a better reproduction of the superadiabatic layers just below the photosphere is similar to the one obtained by using 1d-model atmospheres like in [3]. The advantage of using the 2d- instead of the 1d-model atmospheres is the extension of the former to greater optical depths, where the stratification is already adiabatic and thus the solar model gets nearly independent of the applied convection theory.

In Table I typical quantities of GARSOM4 using the convection theory developed in [41] are summarized. The predicted event rates of GARSOM4 for the three presently operating types of neutrino experiments GALLEX/GNO/SAGE, Homestake, and Super-Kamiokande are summarized in Table II together with the values obtained by [4]. Since the input physics is very similar in both models, the predicted rates agree very well within the errors as quoted by [4]. In addition, the influence of the assumed  $^8\text{B}$ -neutrino spectrum to the predicted rates is shown. Using the recently measured spectrum [17] yields slightly higher rates for all three experiments than including the theoretically predicted one [18], which is caused by the somewhat larger number of high-energetic  $^8\text{B}$ -neutrinos in the former spectrum and the strongly inclining detection probability toward higher energies.

Figure 3 shows the sound-speed profile of GARSOM4 compared to the seismic model inferred by [45]. The

TABLE I. Typical quantities of GARSOM4.  $\alpha_{\text{CM}}$  is the mixing-length parameter of the convection theory developed in [41].  $Y$  and  $Z$  are helium and metal mass fractions,  $T$  and  $\rho$  temperature and mass density, respectively. The depth of the convective envelope in units of the solar radius is abbreviated by  $R_{\text{bce}}$ . The indices  $i$ ,  $s$ , and  $c$  denote initial, surface (photospheric) and central values, respectively.

$\alpha_{\text{CM}}$	$Y_i$	$Z_i$	$Y_s$	$Z_s$	$T_c$ ( $10^7$ K)	$\rho_c$ ( $\text{g}/\text{cm}^3$ )	$R_{\text{bce}}$	$\rho_{\text{bce}}$ ( $\text{g}/\text{cm}^3$ )
0.975	0.275	0.020	0.245	0.018	1.57	152	0.713	0.188

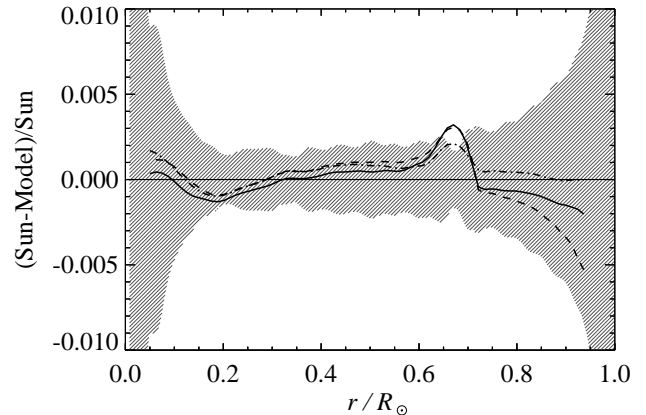


FIG. 3. Comparison of modern solar models with the seismic model by [45]: shown is the relative (seismic-solar model) difference of sound speed for the model of reference [4] (dashed line), reference [46] (dash-dotted), and GARSOM4 (solid). The grey-shaded area indicates a conservative error range of seismic models according to [47].

deviations of GARSOM4 from the latter are of the same size as standard solar models from other groups [4,46].

#### B. Neutrino-oscillation analysis

Using the neutrino flux as provided by GARSOM4 the evolution of the initial electron neutrinos through Sun, space and Earth is computed taking into account oscillations between the flavors (see Appendix). The electron-density profile and the radial distribution of the neutrinos is taken from the solar model, too. For the electron-density profile of the Earth the spherically symmetric PREM-model [48] is applied. For each set of mixing parameters the neutrino energy spectrum observed on Earth is evaluated and folded with the detector response

TABLE II. Expected event rates resp. neutrino flux in the three types of experiments GALLEX/GNO/SAGE (Ga), Homestake (Cl), and Super-Kamiokande as predicted by the two solar models GARSOM4 and BP98 [4]. For GARSOM4 the expected values using the measured [17] (first row) and the theoretically derived [18] (second row)  $^8\text{B}$ -neutrino spectrum are given. The last row provides the the measured values with their respective errors.

	Ga [SNU]	Cl [SNU]	Super-K [ $10^6 \text{cm}^{-2} \text{s}^{-1}$ ]
GARSOM4	128.7	7.79	5.18
	128.4	7.58	5.06
BP98	$129_{-6}^{+8}$	$7.7_{-1.0}^{+1.2}$	$5.15_{-0.72}^{+1.00}$
Experiment	$74.2 \pm 4.9^{\text{a}}$	$2.56 \pm 0.23^{\text{b}}$	$2.40 \pm 0.08^{\text{c}}$

<sup>a</sup>Reference [42]

<sup>b</sup>Reference [43]

<sup>c</sup>Reference [44]

functions. The combinations of mixing parameters which reproduce the measured data are found by applying a  $\chi^2$ -analysis.

There are four contributions to the total value of  $\chi^2$  originating from the four different available data sets, the event rates, the recoil-electron energy spectrum, the zenith-angle distribution, and the annual variation. The latter three are available only from the Super-Kamiokande detector, while to the first one all three types of neutrino experiments contribute.

For the event-rate portion the commonly used formula holds

$$\chi_R^2 = \sum_{i=1}^3 \frac{(N_i^{\text{exp}} - N_i^{\text{th}})^2}{\sigma_{i,\text{exp}}^2 + \sigma_{i,\text{th}}^2}, \quad (15)$$

where  $i$  denotes GALLEX/GNO/SAGE, Homestake or Super-Kamiokande.  $\sigma_{\text{exp}}^2$  and  $\sigma_{\text{th}}^2$  are the experimental resp. theoretical  $1\sigma$ -errors (Table II). Since the input physics in GARSOM4 is similar to the one used in [4], the theoretical errors derived therein are taken for  $\sigma_{\text{th}}^2$ .  $N_i^{\text{exp}}$  are the measured event rates, which are quoted together with the uncertainties in Table II. Note, that the Super-Kamiokande data are usually reported as  ${}^8\text{B}$ -neutrino flux relatively to a standard solar-model prediction. Actually this number has to be understood as an event-rate ratio. The total number of measured events are divided by the theoretically expected value (e.g. from GARSOM4). This ratio is then often falsely taken to be the suppression rate of the *total*  ${}^8\text{B}$ -neutrino flux. However, with the energy window of the recoiled electrons being between 5.5<sup>§</sup> and 20 MeV no statement about the total number of  ${}^8\text{B}$ -neutrinos below this window is possible. Moreover, neutrino oscillations may alter the energy spectrum of the  ${}^8\text{B}$  electron-neutrino flux and as the scattering cross section of the neutrinos in Super-Kamiokande is energy-dependent, the same number of event rates can be obtained with different  ${}^8\text{B}$ -neutrino fluxes. Thus in the present analysis the event rate in Super-Kamiokande following Eq. (A5) are used and not the total  ${}^8\text{B}$ -neutrino flux.

The recoil-electron energy spectrum is examined by

$$\chi_e^2 = \sum_{i=1}^{18} \left( \frac{N_{i,e}^{\text{exp}} - \alpha_e N_{i,e}^{\text{th}}}{\sigma_{i,e}} \right)^2, \quad (16)$$

where the sum extends over all 18 energy bins (Fig. 6(a)) and  $\sigma_{i,e}$  is the quadratic sum of statistical and systematic errors taken from [44]. Since the absolute value of the event rate in Super-Kamiokande has already been used in  $\chi_R^2$  the parameter  $\alpha_e$  is introduced, by which the

<sup>§</sup>There are already data for the energy window from 5.0 to 5.5 MeV available, but the systematic errors are still to be derived.

spectrum can be normalized adequately, independent of the total rates.

The contribution of the zenith-angle dependence (6 bins, Fig. 6(b)) and seasonal-variation data (4 bins, Fig. 6(c)) is defined analogously (denoted in the following  $\chi_Z^2$  resp.  $\chi_A^2$ ).

## IV. RESULTS

### A. Two flavors

In a first step the solar neutrino problem is analyzed taking into account oscillations only between two flavors. Figure 4 shows the allowed oscillation parameters using the experimentally derived  ${}^8\text{B}$ -neutrino spectrum [17], if solely the event rates of the three experiments are fitted. Clearly the four commonly known solution-islands (see

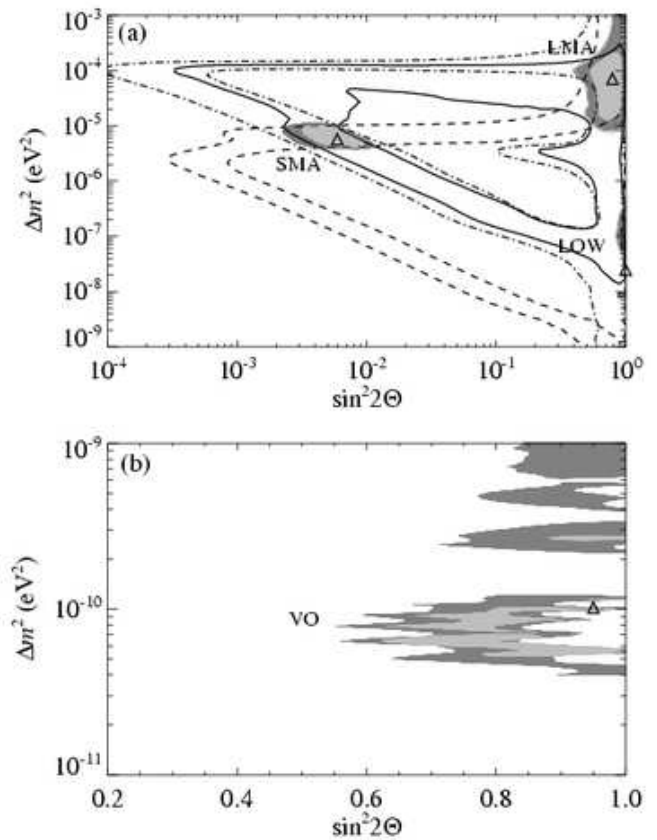


FIG. 4. Confidence regions in the  $\Delta m^2$ - $\sin^2 2\Theta$ -plane for 2-flavor neutrino oscillations using only the event rates. Due to the different mass ranges and dependences on the mixing angle, the MSW-solutions are shown in (a), the pure vacuum-oscillation solutions in (b). The light shaded areas reflect the 95.4% C.L., while the dark shaded regions show the 99.7% C.L. Also drawn in (a) are the constraints from Homestake (solid), GALLEX/GNO/SAGE (dashed), and Super-Kamiokande (dash-dotted line). The best-fit value of each solution is indicated by  $\Delta$  (Table III).

TABLE III. Best-fit values for oscillations between two neutrinos taking into account solely the event rates of the three detector types. In the first four rows the measured  $^8\text{B}$ -neutrino spectrum [17] is included, while in the last rows the spectrum calculated in [18] is assumed. The total number of d.o.f in this analysis is 1.

	$\Delta m^2$ (eV $^2$ )	$\sin^2 2\Theta$	$\chi_{\text{tot}}^2$
SMA	$5.7 \times 10^{-6}$	$5.9 \times 10^{-3}$	0.16
LMA	$7.1 \times 10^{-5}$	0.79	0.79
LOW	$2.5 \times 10^{-8}$	1.00	5.00
VO	$1.0 \times 10^{-10}$	0.95	0.16
SMA	$5.4 \times 10^{-6}$	$6.1 \times 10^{-3}$	0.21
LMA	$7.3 \times 10^{-5}$	0.78	0.81
LOW	$5.0 \times 10^{-8}$	1.00	3.70
VO	$8.1 \times 10^{-11}$	0.73	0.61

e.g. in [12,13]) can be identified, the small-mixing (SMA) and large-mixing angle (LMA), the low mass-squared difference (LOW), and the vacuum-oscillation (VO) solutions. The  $\chi^2$ -values for the best-fit parameters in these solutions are quoted in Table III. Apart from LOW all solutions have a ratio of  $\chi^2$  to the number of degrees-of-freedom (d.o.f.) which is less than one and therefore these solutions are acceptable candidates as correct solution for the solar neutrino puzzle.

In the last four columns in Table III the best-fit values using the theoretically derived  $^8\text{B}$ -neutrino spectrum of reference [18] are provided. The somewhat higher expected event rates (Table II) result in slightly different mixing parameters compared to the case using the measured  $^8\text{B}$ -neutrino spectrum [17] (first four rows). While the  $\chi^2$ -values for the SMA-, LMA-, and VO-solutions are marginally worse with the theoretical spectrum, the LOW-solution give a slightly better fit to the experiments. However the changes are in all cases relatively small.

While the event-rates alone favor the SMA-solution, including into the analysis the recoil-electron energy spectrum, the zenith-angle and annual variations recorded by Super-Kamiokande, yields the LMA-solution as the best fit (Table IV). This result could also be found with the previous 825-day Super-Kamiokande data (see e.g. in [19]). In contrast to the earlier analyses, where no set of parameter could be found, which reproduces all sets of data at the same time [9], with the 1117-days data such simultaneous fits can be performed. In Table IV the best-fit values of these solutions, the respective  $\chi^2$ -contributions and the ratio of  $\chi_{\text{tot}}^2$  to the available d.o.f. are provided.

The 1, 2, and 3 $\sigma$ -regions (63.7, 95.4, and 99.7% C.L.) including all available data (Fig. 5) are much bigger than in the case of taking solely the event rates (Fig. 4). Most probably neglecting the correlations between the different data sets of Super-Kamiokande has caused this growth. More detailed data published from the Super-

TABLE IV. Best-fit values for 2-flavor neutrino oscillations and the respective  $\chi^2$ -values taking into account all available data sets (event rates of GALLEX/GNO/SAGE, Homestake, and Super-Kamiokande and zenith-angle dependence, annual variation, and recoil-electron energy spectrum data of the latter). In the first four rows the measured  $^8\text{B}$ -neutrino spectrum is utilized [17], while in the latter rows the spectrum calculated in [18] is assumed.  $\chi_R^2$ ,  $\chi_e^2$ ,  $\chi_Z^2$  and  $\chi_A^2$  are the individual contributions to  $\chi_{\text{tot}}^2$  as defined by Eqs. (15) and (16). The last row specifies the contribution of each  $\chi^2$ -portion to the total number of d.o.f; the total number of d.o.f in this analysis is 26.

	$\Delta m^2$ (eV $^2$ )	$\sin^2 2\Theta$	$\chi_R^2$	$\chi_e^2$	$\chi_Z^2$	$\chi_A^2$	$\chi_{\text{tot}}^2$ /d.o.f.
SMA	$5.0 \times 10^{-6}$	$3.7 \times 10^{-3}$	6.1	16.2	1.8	1.1	0.97
LMA	$5.3 \times 10^{-5}$	0.79	0.9	8.6	2.0	1.2	0.48
LOW	$1.1 \times 10^{-7}$	0.89	6.0	8.6	2.9	0.1	0.68
VO	$6.9 \times 10^{-10}$	0.95	6.8	8.0	1.9	1.4	0.70
SMA	$5.4 \times 10^{-6}$	$4.2 \times 10^{-3}$	3.3	13.5	2.1	2.0	0.79
LMA	$5.0 \times 10^{-5}$	0.88	2.0	10.9	1.8	1.7	0.63
LOW	$1.0 \times 10^{-7}$	1.00	5.9	10.1	2.7	0.7	0.75
VO	$8.6 \times 10^{-10}$	0.99	6.4	7.9	2.1	1.5	0.68
d.o.f.			3	17	5	3	

Kamiokande collaboration are desirable to be able to perform a more accurate analysis of the solar neutrino data. In addition, theoretical correlations between e.g. the annual and zenith-angle data should be taken into consideration. In order to show, that the most probable solution regions have indeed not changed drastically compared with the pure-rate analysis, the 10% C.L. areas are plotted in Fig. 5, too. The same region would result as the 1 $\sigma$ -area, if the minimum  $\chi_{\text{tot}}^2$ -value would be zero instead of 12.5 (=0.48  $\times$  26, Table IV).

Independent of whether the theoretically derived or measured  $^8\text{B}$ -neutrino spectrum is used, the LMA-solution can reproduce each single kind of data, the event rates, the recoil-electron energy spectrum, the zenith-angle and the seasonal variation acceptably. Although,  $\chi_{\text{tot}}^2$ /d.o.f. of the LOW- and VO-solutions are less than one, these solution do not lead to an acceptable fit of the event-rate data. Whether the SMA-solution can already be ruled out by the new Super-Kamiokande data depends on the  $^8\text{B}$ -neutrino spectrum included in the analysis. While with the theoretically derived spectrum [18], the event rates can just be reproduced ( $\chi_R^2$ /d.o.f.  $\approx$  1), including the measured one [17] hardly yields a reasonable fit.

By assuming that the Chlorine rate is due to unknown systematic errors 30% higher than quoted and by reducing the reaction rate for the  $^7\text{Be}$ -proton capture by about 15–20%, a VO-solution could be obtained which would be able to reproduce the event rates *and* the energy spectrum of Super-Kamiokande fairly well [49]. However, presently there is no evidence for any hidden systematic uncertainties in Homestake, which would increase the event rate to the 3.5 $\sigma$ -level.

The parameters of the best-fit LMA- and SMA-solutions are weakly modified when including all the data in the analysis (Tables III and IV). The recoil-electron

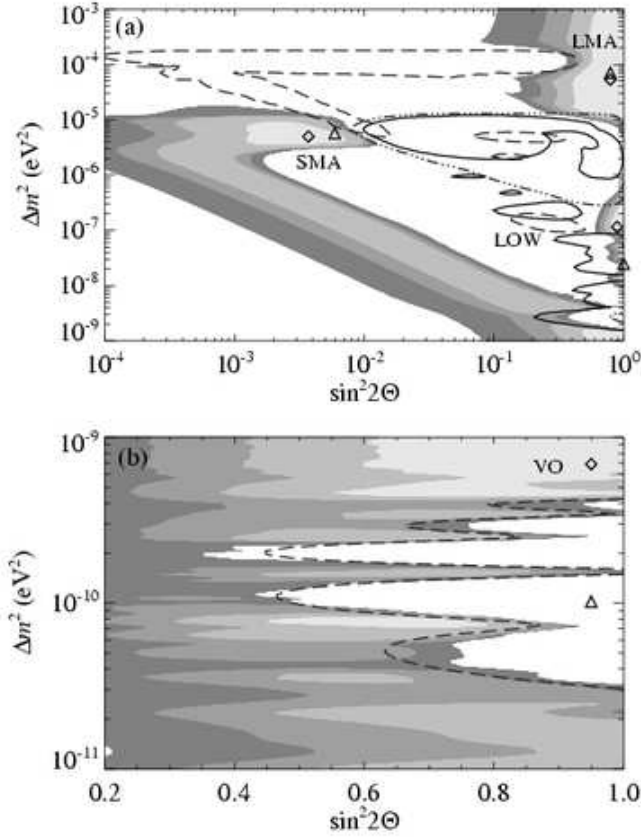


FIG. 5. Confidence regions in the  $\Delta m^2$ - $\sin^2 2\Theta$ -plane for 2-flavor neutrino oscillations using all data. The different shaded areas reflect from light to dark, 10, 63.7, 95.4, and 99.7% C.L. Also drawn in (a) are the constraints from the recoil-electron energy spectrum (dashed), zenith-angle (dashed-dotted) and annual variation (solid line) of the Super-Kamiokande data. The best-fit value of this analysis is indicated by  $\diamond$  (Table IV); the  $\triangle$  show the best-fit values of the analysis taking only the event-rate data (Table III).

energy spectrum mainly influences the SMA-solution, while the zenith-angle data causes a slight shift of the best-fit values of the LMA-solution (Fig. 5).

For  $\Delta m^2 \approx 10^{-7}$ - $10^{-5}$  eV<sup>2</sup> the seasonal variations are caused by the zenith-angle variation (on the northern hemisphere more night data are recorded during winter than during summer), and thus no additional constraints can be obtained from the former data set in this parameter space. For smaller  $\Delta m^2$  the eccentricity of the Earth orbit leads to a “real” annual dependent signal, which can be used to constrain the mixing parameters. Note, that in contrast to the  $\Delta m^2 \gtrsim 10^{-7}$ -region the seasonal dependence in  $\Delta m^2 \lesssim 10^{-7}$  is now producing tiny day-night variations.

Anyway, for  $\Delta m^2 \lesssim 10^{-9}$  eV<sup>2</sup> deviations of less than 2% from an annually constant neutrino flux are predicted

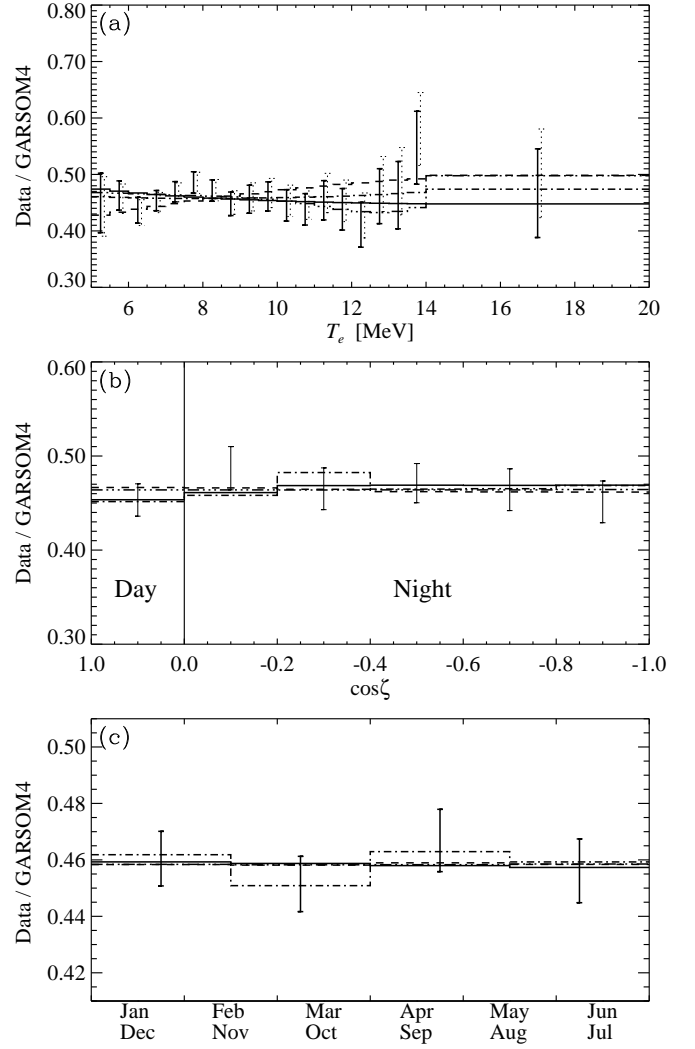


FIG. 6. Recoil-electron energy spectrum (a), zenith-angle ( $\zeta$ ) variation (b), and seasonal dependence of the best-fit LMA- (solid line), SMA- (dashed), LOW- (dash-dotted), and VO- (dash-dot-dot-dotted) solutions in the 2-flavor oscillation case including all available solar neutrino data (Table III, lower part) compared with the measurements of Super-Kamiokande (1117-days data [44]) using the measured <sup>8</sup>B-neutrino spectrum [17] (solid) resp. the theoretically derived one [18] (dotted bins). All bins are equally spaced in the respective data area apart from the last bin in the energy spectrum, the range of which extends from 14 to 20 MeV. The flux variation due to the eccentric orbit of the Earth has been subtracted in (c).

for the Super-Kamiokande data\*\*, which is consistent within the errors with the recorded value. Thus, for the VO-solutions only very weak constraints can be obtained

\*\*In the analysis of the seasonal data the neutrino signal has been corrected for the  $1/r^2$ -dependence of the flux.

from the present seasonal variation data, while for the region of the LOW-solution these data provide important information. In fact, the position of the best-fit value of the LOW-solution has been changed by including the annual-variation data in the analysis (Fig. 5).

In the regime of the VO-solution, the recoil-electron energy spectrum provides very stringent constraints on the allowed mixing parameters, excluding great part of the region favored by the rates. Hence, no good solution in the VO-region could be found, which reproduces the recoil-electron energy spectrum as well as the rates recorded in GALLEX/SAGE/GNO, Homestake, and Super-Kamiokande.

Nevertheless, the LMA-solution is presently the favored solution to the solar neutrino problem, whereas the earlier favored SMA-solution seem to be almost ruled out. But still, improved statistics in the recoil-electron data of Super-Kamiokande is required to identify more reliably the correct solution to the neutrino problem.

## B. Three flavors

In spite of the LMA-solution being able to reproduce the recoil-electron energy spectrum, the zenith-angle and seasonal variations, and the event rates acceptably, the analysis is extended to all three families to deduce whether a better fit to the data can be achieved. Besides, this is the physically correct treatment, which contains the 2-flavor case as a limiting one.

The electron-neutrino survival probability for 3-flavor neutrino oscillations is determined by four quantities  $\Delta m_{12}^2$ ,  $\sin^2 2\Theta_{12}$ ,  $\Delta m_{13}^2$ , and  $\sin^2 2\Theta_{13}$ , where the appropriate pairs describe each the mixing of two flavors. Hence a 4-dimensional parameter space has to be examined to deduce all possible solutions. In the Appendix the numerical realization is described with which the 4-dimensional parameter survey can be performed efficiently. As worked out in section II C, all possible solutions for MSW-solutions are obtained by considering sector I and II (Fig. 2) with  $\Delta m_{12}^2, \Delta m_{13}^2 > 0$ . Using in sector I the quantity  $\sin^2 2\tilde{\Theta}_{13}$  as defined in Eq. (13) instead of  $\sin^2 2\Theta_{13}$ , allows to describe the pure 2-neutrino  $\nu_1$ - $\nu_3$ -oscillations equivalently to the  $\nu_1$ - $\nu_2$ -case, which has been investigated thoroughly in various publications [12,13]. In addition, with the survival probability  $P(r)_{e \rightarrow e}^{(3)}(\Delta m_{12}^2, \sin^2 2\Theta_{12}, \Delta m_{13}^2, \sin^2 2\tilde{\Theta}_{13})$  being symmetric in the exchange of the indices 2 and 3 unnecessary computations can be avoided. Nevertheless, the computations are very extensive due to the 4-dimensional parameter space. Therefore, the grid in the 3-flavor oscillation-survey has to be chosen less dense than in the 2-flavor case, where only a 2-dimensional grid had to be overviewed. However, the grid must still be fine enough that those solutions are not missed which might be confined to small regions in the parameter space. Furthermore, the number of neutrino paths from the Sun to

the detector to cover the whole year of data recording was reduced compared to the pure 2-flavor neutrino oscillations. This leads to slightly different  $\chi^2$ -values for effectively pure 2-flavor solutions, which are also found in the full analysis.

Subspaces of the entire possible parameter space have been investigated e.g. in [20] or [50]. In both publications an analytical expression for the survival probability  $P_{e \rightarrow e}^{(3)}$  derived in [24] has been used, which is valid for large mass separations resp. small mixing angles. In this description  $P_{e \rightarrow e}^{(3)}$  is determined by two 2-flavor probabilities  $P_{e \rightarrow e}^{(2)}$  for each mass splitting  $\Delta m_{12}^2$  and  $\Delta m_{13}^2$ . By approximating the electron-density profile in the solar interior with an exponential function,  $P_{e \rightarrow e}^{(2)}$  can also be evaluated analytically [24].

The results obtained in [20] or [50] could always be reproduced in the respective mass ranges. However, in those investigations of the 3-flavor scenario, only the event-rate data were available. Using the new type of data (recoil-electron energy spectrum, zenith-angle and seasonal variations) almost all solutions found in [20,50] are disfavored. Furthermore, new solutions are identified since the respective parts of the parameter space were not covered in the analyses therein.

In the  $\chi^2$ -analysis, applied to constrain the mixing parameters, always the whole available experimental data set was used for the present study. Furthermore, solely the measured  $^8\text{B}$ -neutrino spectrum [17] has been included. The  $\Delta m_{12}^2$ - $\Delta m_{13}^2$ -plane is divided according to the 2-flavor case in three subregions where the two oscillation-branches  $\nu_1 \leftrightarrow \nu_2$  and  $\nu_1 \leftrightarrow \nu_3$  are either both of matter type, or both of vacuum type, or one of matter and the second of vacuum nature.

### 1. Oscillations in the MSW mass regime

First sector I is investigated, where  $\nu_1 \leftrightarrow \nu_2$  and  $\nu_1 \leftrightarrow \nu_3$  both may undergo resonant MSW-transition, i.e.  $10^{-9} \leq \Delta m_{12}^2, \Delta m_{13}^2 \leq 10^{-3} \text{ eV}^2$ . In Fig. 7 the projection of the region with  $\chi^2 \leq 26.5$  on the 3-dimensional subspace  $\sin^2 2\Theta_{12}$ - $\Delta m_{13}^2$ - $\sin^2 2\tilde{\Theta}_{13}$  is shown. The allowed parameters are located within the grey-shaded surroundings.

The pure 2-flavor  $\nu_1 \leftrightarrow \nu_3$  oscillations where the mixing into  $\nu_2$  is negligible are given by vertical structures. For instance, the LMA- and LOW-solutions are represented by the half-pillars at  $\sin^2 2\tilde{\Theta}_{13} = 1$  and  $\Delta m_{13}^2 \approx 5 \times 10^{-5}$  and  $10^{-7} \text{ eV}^2$ . The horizontal planes provide the solutions independent of  $\nu_3$ , and thus are 2-flavor oscillations in the  $1 \leftrightarrow 2$  system, where the influence from  $\Delta m_{12}^2$  is not visible. However, the symmetry of sector I in the exchange of the indices 2 and 3 implies that they must be equivalent to solutions independent of  $\nu_2$ . Therefore, the plane around  $\sin^2 2\Theta_{12} \approx 1$  is equivalent to the pillar-like structures at  $\sin^2 2\tilde{\Theta}_{13} = 1$  and can thus be identified as an overlap of mainly LMA- and LOW-solutions. Similarly the plane at  $\sin^2 2\Theta_{12} \approx 3 \times 10^{-3}$  represents the

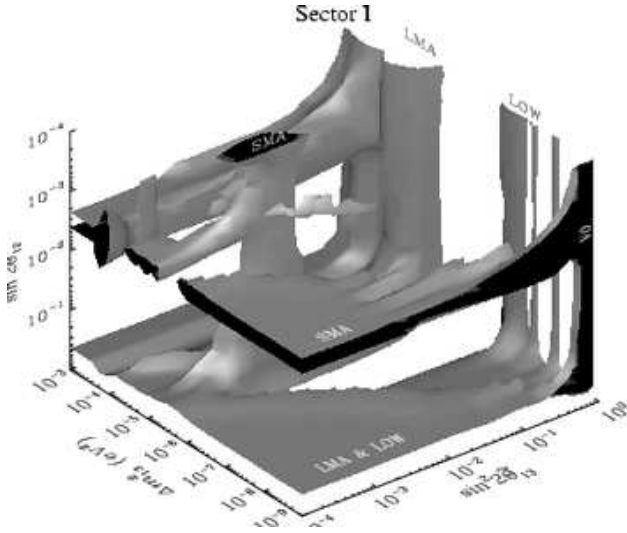


FIG. 7. Shaded volume representing the projection of the region with  $\chi^2 \leq 26.5$  into the 3-dimensional subspace of  $\sin^2 2\Theta_{12}-\Delta m_{13}^2-\sin^2 2\tilde{\Theta}_{13}$  for MSW-transitions in the  $\nu_1 \leftrightarrow \nu_2$  and  $\nu_1 \leftrightarrow \nu_3$  system (sector I). The allowed values are located within the light shaded surroundings. The position of the classical 2-flavor solutions are also shown, which may be in the  $1 \leftrightarrow 2$  as well as in the  $1 \leftrightarrow 3$  system.

SMA-solution. The 3-flavor solutions with the smallest  $\chi^2$ -values are sited near the intersection regions of the horizontal planes and vertical objects, which means that they are at least slightly more probable than the pure 2-flavor solutions and involve indeed all three flavors.

In Fig. 8 the regions with  $\chi^2 \leq 15.4$  of the present sur-

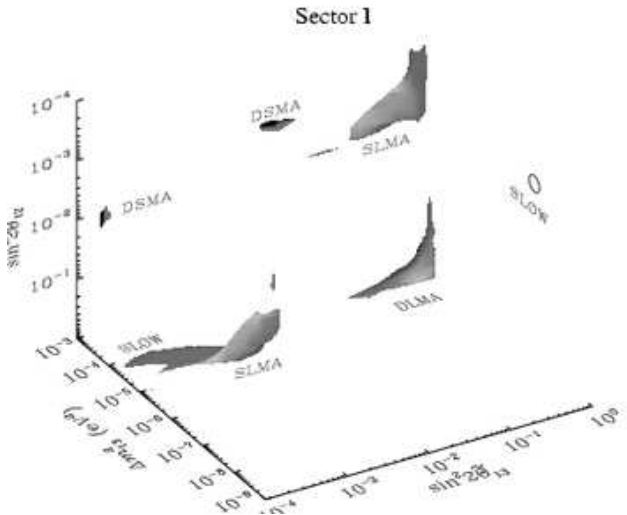


FIG. 8. Zoom into the shaded volume of Fig. 7 showing the position of the SLMA-, DSMA-, DLMA-, and SLOW-solutions. The shaded bodies enclose the regions with  $\chi^2 \leq 15.4$ . The circle in the  $\sin^2 2\Theta_{12}-\Delta m_{13}^2$ -plane at  $\sin^2 2\tilde{\Theta}_{13} = 1$  shows the position of the tiny solution area of SLOW.

vey are shown. Due to the symmetry in  $\nu_2 \leftrightarrow \nu_3$  and the overlap of solution islands in this projection the 6 basic regions in this figure belong only to four distinct solutions. Two of them can be identified as “double” SMA-resp. LMA-solutions, i.e. the same kind of solution in  $\nu_1 \leftrightarrow \nu_2$  and  $\nu_1 \leftrightarrow \nu_3$  (DSMA resp. DLMA). In addition, two solutions are combinations of a SMA-solution in  $\nu_1 \leftrightarrow \nu_2$  ( $\sin^2 2\Theta_{12} \lesssim 10^{-3}$ ) and a LMA resp. LOW in  $\nu_1 \leftrightarrow \nu_3$  ( $\sin^2 2\tilde{\Theta}_{13} \gtrsim 10^{-1}$  and  $\Delta m_{13}^2 \approx 10^{-4}$  resp.  $10^{-7}$  eV<sup>2</sup>), therefore denoted SLMA and SLOW. The extension of the SLOW-solution in the  $\sin^2 2\Theta_{12}-\Delta m_{13}^2$ -plane at  $\sin^2 2\tilde{\Theta}_{13} \approx 1$  is very small and thus its position is marked by a small circle. The assignment of  $\nu_1 \leftrightarrow \nu_2$  to SMA and  $\nu_1 \leftrightarrow \nu_3$  to LMA resp. LOW is ambiguous and could also be chosen vice versa. This is reflected by the second appearance of the SLOW- and SLMA-solutions in Fig. 8 at  $\sin^2 2\Theta_{12} \gtrsim 10^{-1}$  and  $\sin^2 2\tilde{\Theta}_{13} \lesssim 10^{-3}$ . The respective solution islands merge in this projection.

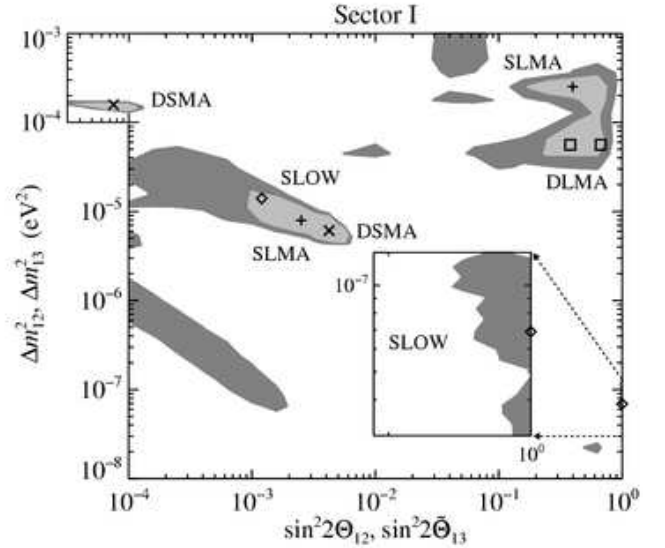


FIG. 9. Projection of the DSMA-, DLMA-, SLMA-, and SLOW-solutions onto the  $\Delta m_{12}^2-\sin^2 2\Theta_{12}$ - or the  $\Delta m_{13}^2-\sin^2 2\tilde{\Theta}_{13}$ -plane. The dark and bright shaded areas show the regions of  $\chi^2 \leq 15.6$  and  $13.9$ . Following the assignment of Table V, the  $\chi^2 \leq 13.9$ -region of the DSMA-, SLMA-, and SLOW-solutions merge in the projection onto the  $\Delta m_{12}^2-\sin^2 2\Theta_{12}$ -plane, but are well separated in the  $\Delta m_{13}^2-\sin^2 2\tilde{\Theta}_{13}$ -plane (see also Fig. 8). The region with  $\sin^2 2\tilde{\Theta}_{13} < 10^{-4}$  has been scanned separately only near the DSMA-solution ( $10^{-6} < \Delta m_{12}^2 < 10^{-4}$  eV<sup>2</sup> and  $10^{-4} < \sin^2 2\Theta_{12} < 10^{-2}$ ).

In Fig. 9 the projection of the DSMA-, DLMA-, SLMA-, and SLOW-solutions into the typical 2-flavor planes are shown. One of the areas labelled, for instance, SLMA has to be identified with oscillations in  $\nu_1 \leftrightarrow \nu_2$  and the other with  $\nu_1-\nu_3$ -mixing. The oscillation parameters are provided in Table V together with the  $\chi^2$ -values. Since two more parameters are adjusted

in the 3-neutrino as compared to the 2-neutrino case, the number of degrees-of-freedom reduces from 26 to 24.

The mixing angle of the second small mixing-angle branch in the DSMA-solution at  $\sin^2 2\tilde{\Theta}_{13}$  is about two order of magnitude smaller than the usual 2-flavor SMA-solution (compare Figs. 9 and 4). This second SMA-branch causes an additional resonance at  $E \approx 10$  MeV (see Fig. 10), which enables a better fit to the recoil-electron energy spectrum and the event rates (compare Tables IV and V). Thus a solution almost as good as the LMA-solution could be obtained ( $\chi_{\text{tot}}^2/\text{d.o.f.} = 0.5$ ).

The DLMA- and SLMA-solutions have almost the same values for  $\chi_R^2$ ,  $\chi_e^2$ ,  $\chi_Z^2$  and  $\chi_A^2$  as the LMA-solution (cp. Tables IV and V). Since thus no improvement in explaining the solar neutrino measurements could be achieved by combining the LMA-solution with an additional oscillation in the  $\nu_1 \leftrightarrow \nu_3$ -system, the 2-flavor LMA-solution itself is a favored solution in the 3-flavor analysis, too

In the SLOW-solution the advantages of the 2-flavor

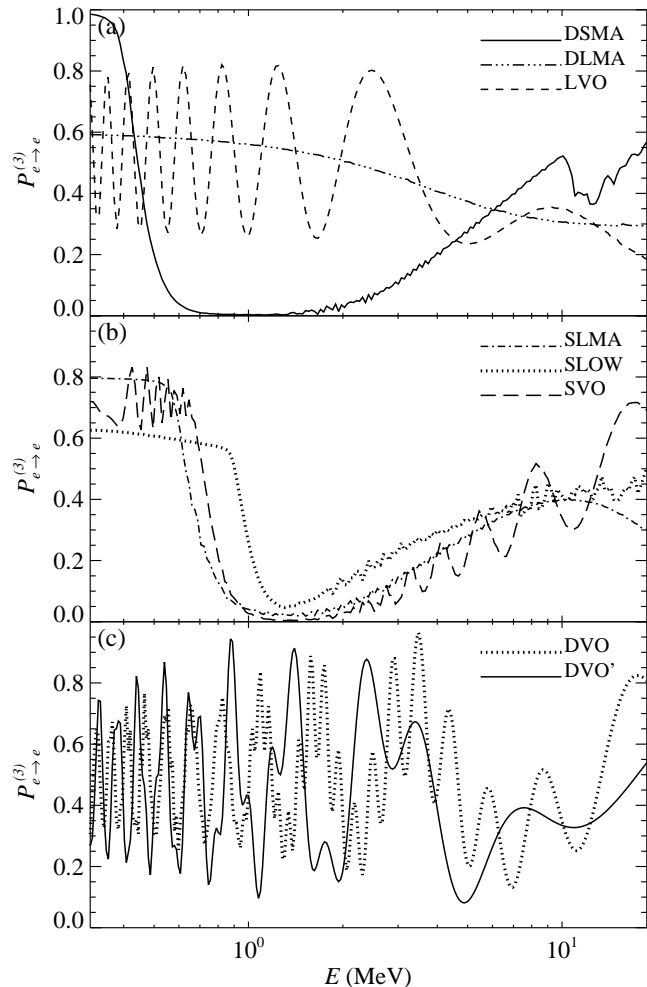


FIG. 10. The annually averaged survival probability of  ${}^8\text{B}$  electron-neutrinos detected on Earth for the deduced 3-flavor solutions.

SMA- and LOW-solutions are united. While with the SMA-solution the rates can be reproduced very well (see Table III), the LOW-solution provides good fits to the energy spectrum, the annual and the zenith angle variations (Table IV).

The best-fit value of the SLOW-solution for  $\sin^2 2\tilde{\Theta}_{13}$  is equal to 1, and thus at the border of sector I to sector III. Exchanging the assignment of the indices 2 and 3 transfers the SLOW-solution to the border between sector I and II. In the latter sector, where  $\pi/4 \leq \sin \Theta_{12} \leq \pi/2$  and  $\tan \Theta_{13} \leq \sin \Theta_{12}$  a survey has been performed, too. However no new solutions could be identified; solely, the “foothills” of the SLOW-solution into this section have been found. Hence, in the mass regime with  $10^{-9} \leq \Delta m_{12}^2, \Delta m_{13}^2 \leq 10^{-3} \text{ eV}^2$  the region with  $\pi/4 \leq \sin \Theta_{12} \leq \pi/2$  does not provide new solutions, which is similar to the findings in the 2-flavor case, where also no additional solutions have been detected in this parameter range.

## 2. Three-flavor vacuum oscillations

In the case when both mass-squared differences are in the vacuum-oscillation regime ( $\Delta m_{12}^2, \Delta m_{13}^2 \leq 10^{-9} \text{ eV}^2$ ) two minima could be found, denoted DVO and DVO'. While DVO is located in sector I (Fig. 11), i.e.  $0 \leq \Theta_{12} \leq \pi/4$ , DVO' has been found in sector II (Fig. 12), where  $\pi/4 < \Theta_{12} \leq \pi/2$ . Thus although they seem to have very similar mixing parameters (Table V), there are really distinct solutions with different properties (see Fig. 10). Note that, while in sector I the assignment of the indices can be exchanged, this is not possible in sector II. If an

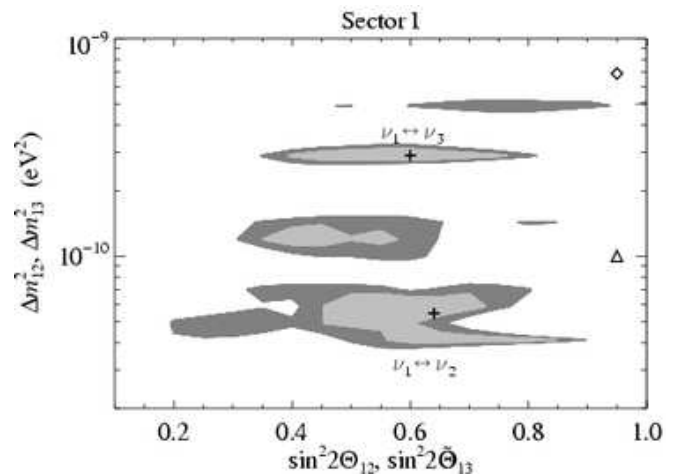


FIG. 11. Projection of the DVO-solution on the  $\Delta m_{12}^2 - \sin^2 2\Theta_{12}$ - resp.  $\Delta m_{13}^2 - \sin^2 2\tilde{\Theta}_{13}$ -plane. The  $\chi^2$ -levels of the regions agree with those of Fig. 9 and the “+”-symbols denote the best-fit values. The best-fit value of the 2-flavor VO-solution reproducing solely the event rates is marked by  $\Delta$ , while the position of the 2-flavor VO-solution in the complete analysis is shown by  $\circ$ .

TABLE V. The most favored solutions within the 3-flavor oscillation scenario and the respective  $\chi^2$ -values. The second column indicates the sector in the flavor space, where the solution has been found (see also Fig. 2).  $\Delta m_{ij}^2$  is in units of  $\text{eV}^2$  and  $s_{ij}^2$  abbreviates here  $\sin^2 2\Theta_{ij}$ . In sector I  $\sin^2 2\tilde{\Theta}_{13}$  is defined by Eq. (13), analogously in sector II by Eq. (14).  $\chi_R^2$ ,  $\chi_e^2$ ,  $\chi_Z^2$  and  $\chi_A^2$  are the individual contributions to  $\chi_{\text{tot}}^2$  as defined by Eqs. (15) and (16). The number of d.o.f. is 24.

		$\Delta m_{12}^2$	$s_{12}^2$	$\Delta m_{13}^2$	$\tilde{s}_{13}^2$	$\chi_R^2$	$\chi_e^2$	$\chi_Z^2$	$\chi_A^2$	$\chi_{\text{tot}}^2/\text{d.o.f.}$
DSMA	I	$6.1 \times 10^{-6}$	$4.2 \times 10^{-3}$	$1.6 \times 10^{-5}$	$7.5 \times 10^{-5}$	0.6	8.2	1.9	1.2	0.50
DLMA	I	$5.6 \times 10^{-5}$	0.67	$5.6 \times 10^{-5}$	0.38	0.9	8.5	2.0	1.3	0.53
SLMA	I	$7.9 \times 10^{-6}$	$2.5 \times 10^{-3}$	$2.5 \times 10^{-4}$	0.40	0.6	8.5	1.8	1.1	0.50
SLOW	I	$1.4 \times 10^{-5}$	$1.2 \times 10^{-3}$	$6.9 \times 10^{-8}$	1.00	1.8	8.7	2.1	2.1	0.61
DVO	I	$5.5 \times 10^{-11}$	0.64	$2.9 \times 10^{-10}$	0.60	3.5	5.7	1.9	1.5	0.53
DVO'	II	$1.2 \times 10^{-10}$	0.58	$7.3 \times 10^{-11}$	0.79	2.3	6.8	1.9	1.5	0.52
SVO	I	$2.7 \times 10^{-10}$	0.51	$1.0 \times 10^{-5}$	$2.5 \times 10^{-3}$	1.6	5.9	1.8	0.9	0.43
LVO	I	$4.1 \times 10^{-11}$	0.70	$1.7 \times 10^{-4}$	0.40	1.4	8.1	2.0	2.0	0.56
d.o.f.						3	17	5	3	

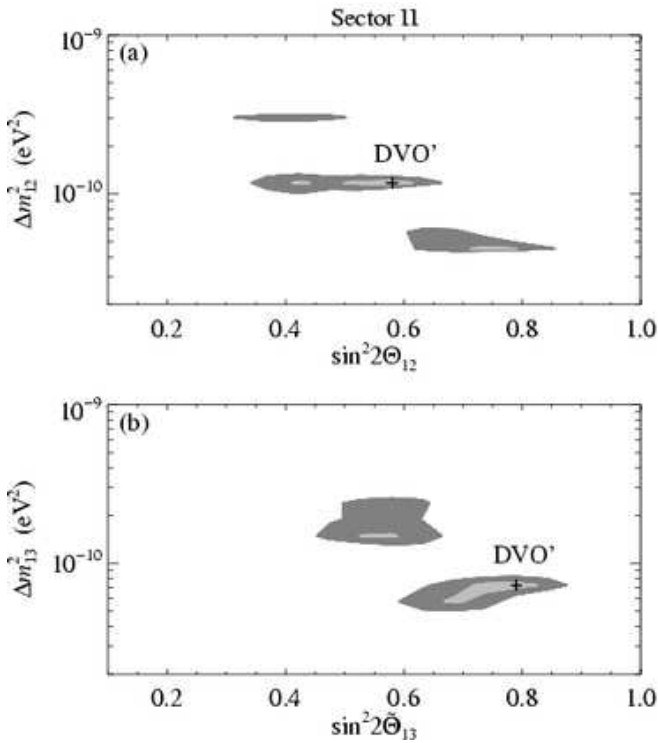


FIG. 12. Projection of the DVO'-solution on the  $\Delta m_{12}^2$ - $\sin^2 2\Theta_{12}$ - and  $\Delta m_{13}^2$ - $\sin^2 2\tilde{\Theta}_{13}$ -plane. The  $\chi^2$ -levels of the regions agree with those of Fig. 11.

exchange of  $\nu_2$  and  $\nu_3$  in DVO' is desired, the mixing angles have to be transformed appropriately to lie finally in sector III.

With the DVO- and DVO'-solutions a slightly better fit to the recoil-electron energy spectrum can be achieved compared to the DSMA-, DLMA-, and SLMA-solutions (Table V). However, because of the event rates being reproduced worse, the  $\chi_{\text{tot}}^2$ -values of DVO and DVO' are almost equal to the values of DSMA, DLMA, and SLMA.

Compared to the 2-flavor VO-solution an improved fit to the event rates has been obtained with the 3-

flavor vacuum-oscillation solutions, but still the event rates are fitted barely acceptably. The DVO- and DVO'-solutions show a compromise between the VO-solution ( $\Delta$  in Fig. 11) obtained by fitting solely the event-rate data and the VO-solution of the complete analysis ( $\diamond$  in same figure). The mixing angles for the 3-flavor vacuum solution are only about one half of the usual 2-flavor VO-solution, as  $\nu_e$  is now oscillating nearly equally strong into *two* other flavors.

### 3. Mixed vacuum and MSW oscillations

The combination of oscillation between two neutrino flavors in the MSW mass-regime and an additional vacuum oscillation into the third flavor is investigated completing the mass ranges which have not been covered by the previous sections. This case has been examined in [50] for  $10^{-7} \leq \Delta m_{13}^2 \leq 10^{-4} \text{eV}^2$  and  $10^{-12} \leq \Delta m_{12}^2 \leq 10^{-9} \text{eV}^2$ . However, in that analysis only the event rates have been included, but not the recoil-electron energy spectrum, the zenith-angle dependence nor the annual variation data recorded by Super-Kamiokande. Furthermore, the Earth-regeneration effect has been neglected. Therefore, this case is reinvestigated including all the available data and calculating the electron-neutrino survival probabilities fully consistently including the Earth effect like in the previous sections.

In this survey  $\Delta m_{13}^2$  is taken to be in the mass range of the MSW-solutions ( $10^{-9} \leq \Delta m_{13}^2 \leq 10^{-3} \text{eV}^2$ ) and  $\Delta m_{12}^2$  in the vacuum oscillation area ( $10^{-12} \leq \Delta m_{12}^2 \leq 10^{-9} \text{eV}^2$ ). With these conventions about  $\Delta m_{13}^2$ , two possibilities are conceivable for the  $\nu_1 \leftrightarrow \nu_3$  system, a resonant and a non-resonant oscillation. Since the masses are well separated, the condition for a resonance obtained in the 2-flavor case can be applied (Eq. 11)

$$N_{\text{res}} = \frac{\Delta m_{13}^2/2E}{\sqrt{2}G_F} \cos 2\Theta_{13} > 0.$$

Thus, an MSW flavor transition is only possible, if the

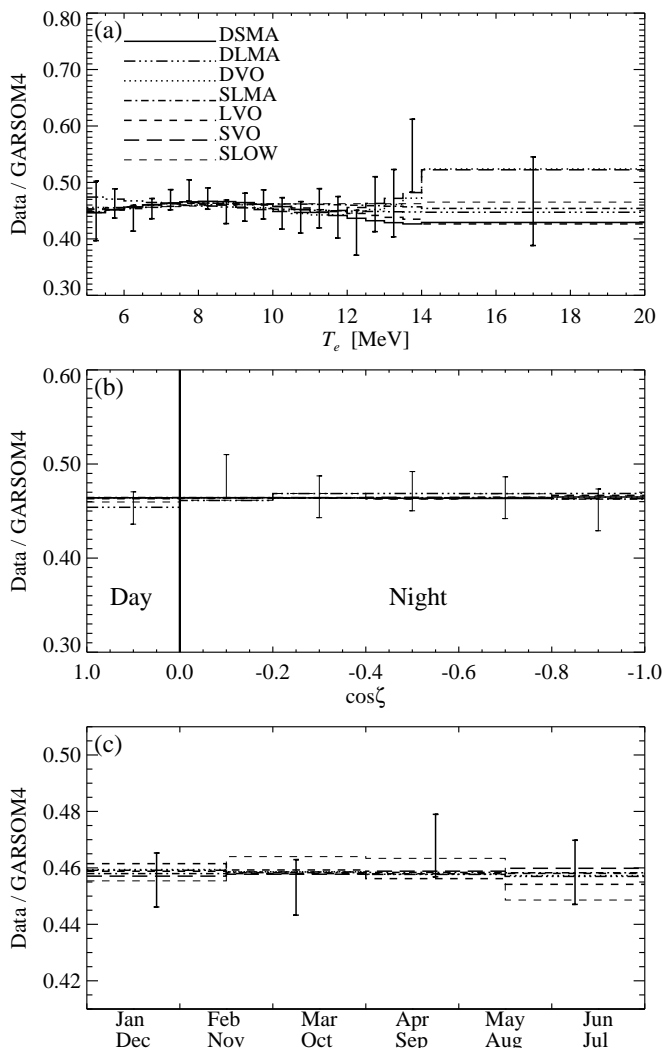


FIG. 13. Recoil-electron energy spectrum (a), zenith-angle variation (b), and seasonal dependence (c) of the best fit 3-flavor solutions including all available solar neutrino data compared with the measurements of Super-Kamiokande. The experimental data agree with Fig. 6 using the measured  $^8\text{B}$ -neutrino spectrum [17].

mixing angle  $\Theta_{13}$  is less than  $\pi/4$ . In the  $\nu_1 \leftrightarrow \nu_2$  system only pure vacuum oscillations occur, and thus  $\Theta_{12} \leq \pi/4$ . Since the solution may be a combination of a vacuum oscillation in the  $1 \leftrightarrow 2$  and a resonant resp. non-resonant oscillation in the  $1 \leftrightarrow 3$  branch, the complete essential parameter space for  $10^{-9} \leq \Delta m_{13}^2 \leq 10^{-3} \text{ eV}^2$  and  $10^{-12} \leq \Delta m_{12}^2 \leq 10^{-9} \text{ eV}^2$  is therefore covered by  $\Theta_{12} \leq \pi/4$  and  $\Theta_{13} \leq \pi/2$ .

Basically two minima could be found in the parameter space of this subsurvey, which are combinations of a SMA- resp. a LMA-solution in  $\nu_1 \leftrightarrow \nu_3$  ( $\Theta_{13} \leq \pi/4$ ) and an additional VO-mixing in  $\nu_1 \leftrightarrow \nu_2$ , therefore denoted SVO and LVO. The SVO-solution is similar to the solution “B” found in [50]. Interestingly, the vicinity of the SVO-solution has been explored intensively in [51],

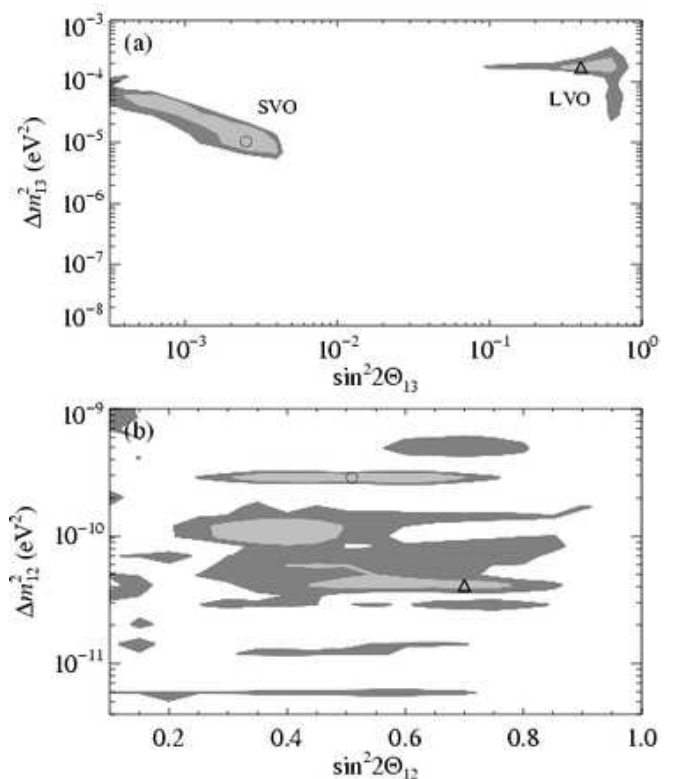


FIG. 14. Projections of the SVO- and LVO-solutions onto the  $\Delta m_{12}^2$ - $\sin^2 2\Theta_{12}$ - and  $\Delta m_{13}^2$ - $\sin^2 2\Theta_{13}$ -plane. The  $\chi^2$ -levels are chosen to be 13.9 (bright) and 15.6 (dark shaded) like in the previous figures. The circles mark the best-fit values of the SVO-solution, the triangles the one of the LVO-solution. ( $\Theta_{12}, \Theta_{13} \leq \pi/4$ )

whereas the motivation was different: The mixing parameters of this solution agree with the neutrino properties predicted by a grand unification (GU) theory, where the neutrino masses are caused by the seesaw mechanism with the mass of the heaviest right-handed neutrino being of the order of the GU-scale.

The fit of the LVO-solution to the data is worse than the pure 2-flavor LMA-solution supporting the result of part 1 of this section, that the LMA-solution cannot be improved by including a third oscillation. However, the mass-squared difference of the LMA-branch in the LVO- as well as in the SLMA-solution ( $\Delta m_{13}^2 \approx 2 \times 10^{-4} \text{ eV}^2$ ) is almost one order of magnitude higher than that of the LMA-solution itself. The implication of this fact for the combined analysis of solar and atmospheric neutrino problem will be discussed further in the final section.

The SVO-solution is presently the favored solution to the solar neutrino problem, in contrast to all other 3-flavor solutions even better than the 2-flavor LMA-solution. SVO combines the merit of the VO-solution to explain the energy spectrum and the property of the SMA-solution to reproduce the event rates (Table III). Interestingly, this solution has also been found to be the best explanation of the solar neutrino problem, using the

older 504- or 708-days data sets of Super-Kamiokande.

## V. PROSPECTS FOR FUTURE EXPERIMENTS

Future neutrino experiments like SNO or Borexino will provide further information to determine the correct solution to the solar neutrino problem. In the following the ability of these detectors to discriminate the various 2- and 3-flavor solutions will be discussed.

### A. Borexino

In Fig. 16 the expected recoil-electron energy spectrum in Borexino of the 2- and 3-flavor solutions is shown. The shades and hatched areas indicate the uncertainties in the mixing parameters of the four 2-flavor solutions. These areas were obtained by allowing the mixing parameters to vary within the 10% confidence region of the  $\Delta m^2$ - $\sin^2 2\theta$ -plane (see Fig. 5).

While in the presently operating detectors, the  ${}^7\text{Be}$ -neutrinos contribute, if at all, only a small portion to the total event rate, Borexino is going to measure basically these neutrinos (Fig. 15). In addition, the highest energy bin of the recoil-electron spectrum ( $T_e \geq 0.75$  MeV) is sensitive to the neutrinos of the CNO-cycle and of the pep-reaction. Borexino may also measure the high energy part of the pp-neutrino spectrum, as these may contribute about 9% to the total rate in the lowest energy bin ( $T_e \leq 0.3$  MeV).

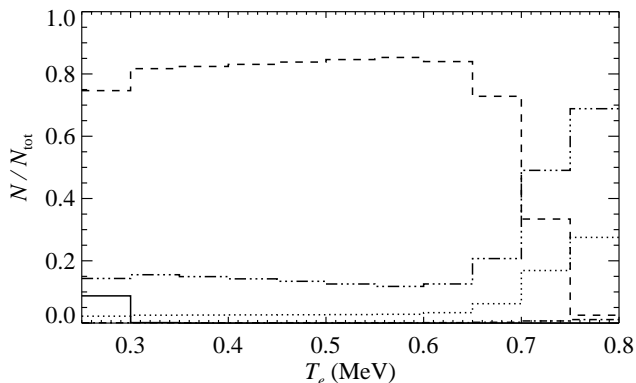


FIG. 15. The contribution of different neutrino types to the total event rate in Borexino in the case of no oscillations. The neutrino flux was derived from GARSOM4. The linestyles correspond to pp- (solid), pep- (dotted),  ${}^7\text{Be}$ - (dashed), CNO- (dash-dot-dot-dotted), and  ${}^8\text{B}$ -neutrinos (dash-dotted).

In the case of the SMA-solution Borexino should detect only about 25% of the event rate as predicted by GARSOM4, while in the LMA-case about 65% are expected (Fig. 16). Actually, for the SMA-solution the rate is basically due to the interaction of the  $\nu_\mu$  (or  $\nu_\tau$ ) with the

detector, as in this solution the  ${}^7\text{Be}$ -neutrinos almost totally consist of  $\nu_\mu$ -flavor. This leads to an unmistakable signal of the SMA compared to the LMA-solution: An excess in the lowest energy bin of about 30% compared to the other bins caused by the pp-neutrinos. With the resonance in the SMA-solution being at about 0.3 MeV, pp-neutrinos do, unlike  ${}^7\text{Be}$ - or CNO-neutrinos, not undergo an MSW-transition. Thus, with good statistics in the low energy bins SMA could be clearly distinguished from LMA.

One of the main advantages of this detector is the ability to monitor seasonal variations in the neutrino signal — the vacuum survival probability is modified by the eccentric orbit of the Earth (Eq. 10). Since the  ${}^7\text{Be}$ -neutrinos are in contrast to  ${}^8\text{B}$ -neutrinos emitted to 90% in a monoenergetic line at 0.862 MeV the signal in the detector is not smeared out like in Super-Kamiokande. A detailed analysis about the sensitivity of Borexino to detect vacuum oscillations is given in [52].

The sensitivity of the  ${}^7\text{Be}$ -neutrino flux in the VO-regime is also visible in the zenith-angle dependence of the event rate in Borexino (thin solid line in Fig. 17(b)). In particular, the rates of those zenith angles, under which the Sun appears only around the winter or summer solstice ( $|\cos \zeta| \gtrsim 0.6$ ), are influenced by the modulation of the  ${}^7\text{Be}$ -neutrino signal with the Sun-Earth distance. Note that unlike the Earth regeneration effect, which in the MSW mass-range can lead to a variation of

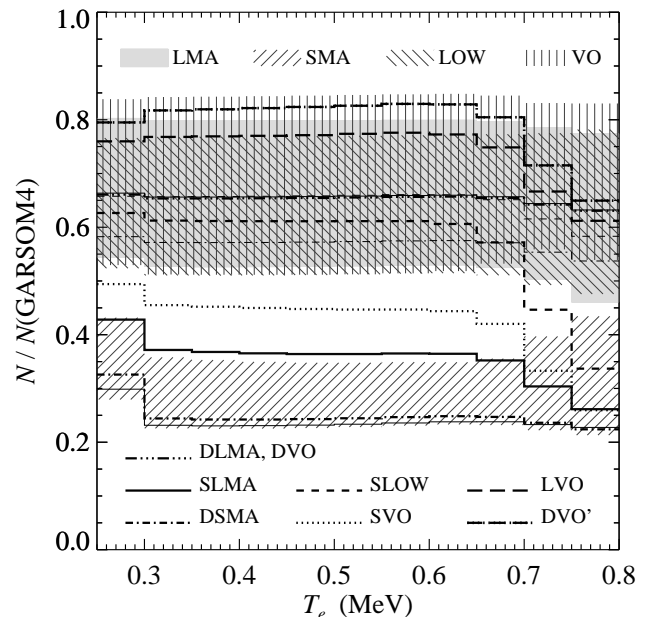


FIG. 16. Expected recoil-electron energy spectrum in Borexino for the best-fit 2- and 3-flavor solutions. The shaded and hatched areas have been obtained by allowing the mixing parameters to vary within the 10%-region of the 2-flavor LMA resp. SMA-solution shown in Fig. 5. The thin lines represent the best-fit 2-flavor solutions in the respective area (solid: SMA resp. LMA, dash-dotted: LOW, dashed line: VO).

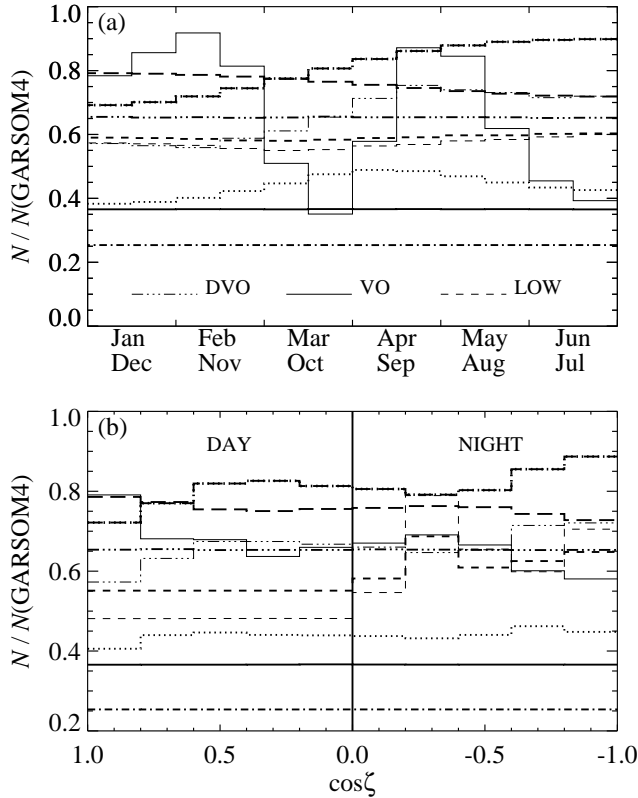


FIG. 17. Annual and zenith-angle variations of the recoil electrons in Borexino expected for the best-fit 3-flavor solutions. The thick lines correspond to same solutions as in Fig. 16. In the seasonal variation (b) the flux changes due to the eccentricity of the Earth’s orbit have been subtracted.

the event rate with the zenith angle only during the night (see thin dash-dotted line in Fig. 17(b) representing the LOW-solution), for VO-solutions a variation in the signal over the whole day is apparent. The magnitude of the zenith-angle variation however is smaller, as each zenith-angle bin is an average over many positions of the Earth in its solar orbit. Therefore, the seasonal variation of the event rates are more sensitive to detect VO-solutions as the zenith-angle dependence. For the best-fit mixing parameters of the MSW-solutions SMA and LMA no Earth regeneration takes place for the energy of the  ${}^7\text{Be}$ -neutrinos, and thus no zenith-angle variation of the event rates in Borexino is expected for these cases. In case of the LOW-solution, however, day-night variations should be measured (thin dash-dotted line in Fig. 17(b)).

In summary for the 2-flavor case, a total rate of about  $30 \pm 5\%$  compared to GARSOM4 is predicted for the SMA-solution, and about  $65 \pm 15\%$  for the LMA-, LOW-, and VO-solutions. The latter three can be disentangles by using the zenith-angle and seasonal data. Great seasonal variations are expected for the VO-solution, strong zenith-angle dependence during the night for LOW, and a constant neutrino flux during the whole year for the LMA-solution, provided that the influence of the eccen-

tric Earth orbit has been removed. Note, that also for the SMA-solution neither zenith-angle nor seasonal variations are expected.

The expected energy, zenith-angle, and seasonal dependences of the recoil electrons in Borexino for the best-fit values of the eight 3-flavor solutions are shown in Figs. 16 and 17, too. The DSMA and DLMA cause very similar signals as their 2-flavor counterparts SMA resp. LMA, and are therefore difficult to disentangle from the latter in any kind of the Borexino data.

But the SLOW-solution leads to a clear signature in Borexino compared to the 2-flavor solutions. It has a strongly reduced event rate of almost 50% in the high-energy bins of Borexino, which are not observed in any other solution. The reason for this is the relatively high resonance energy of about 1 MeV (cf. Fig. 10), which causes a strong suppression of electron-type CNO- and pep-neutrinos, but a weaker reduction of  ${}^7\text{Be}$  electron-neutrinos. By way of contrast, the resonances of the SLMA- and SVO-solutions are about 0.8 MeV (Fig. 10), and thus, the  ${}^7\text{Be}$  electron-neutrino are diminished stronger than in the SLOW-solution, which according to Fig. 15 yields smaller rates below 0.7 MeV.

In addition, the SLOW-solution leads to a zenith-angle dependent signal during the night due to the Earth regeneration effect (Fig. 17(b)) caused by the LOW-branch of this solution. Thus, a large day-night variation measured by Borexino would strongly favor LOW or SLOW. By additional data from the energy spectrum these solution should then be distinguishable from each other.

The mean event rates expected for the SLMA- and SVO-solutions are within a region, where all other solutions are disfavored. Since for the SVO-solution also annual variations are expected from its VO-branch (see Fig. 17(a)), both solutions may be disentangled from each other and from all other solutions.

The properties of the pure 3-flavor vacuum-oscillation solutions DVO and DVO’ are very sensitive to the exact mixing parameters. Even a very small variation in the mixing parameters of these solutions may produce a recoil-electron energy spectrum or seasonal changes which resembles that of the other or the LVO-solution. Hence a discrimination between DVO, DVO’, and LVO will almost be impossible with Borexino.

These solutions are also difficult to distinguish from the 2-flavor VO-solution. However, the most probable value for  $\Delta m^2$  of the VO-solution is almost one order of magnitude larger than the VO-branch(es) of DVO, DVO’ or LVO (compare Tables IV and V) yielding a more frequently varying annual signal for the VO-solution. Hence, measuring a weak annually varying signal with only one maximum per half of the year would at least provide a strong hint, that the solution to the solar neutrino problem is rather a 3-flavor DVO-, DVO’- or LVO-solution than a pure 2-flavor VO solution.

## B. SNO

Recently, SNO has started to measure solar neutrinos in the same energy window as Super-Kamiokande, however with a better energy resolution and the ability to discriminate the CC- and NC-events. Since the total number of neutrinos does not change by neutrino oscillations (only their flavor), the number of NC-events has to agree with the no-oscillation scenario, i.e. the total number of solar neutrinos independent of their flavor can be determined by this quantity<sup>††</sup>. Therefore, no departures in the recoil-deuterium energy spectrum, zenith-angle or seasonal dependence from the standard (no-oscillation) values are expected for NC-events. The merit of SNO is the measurement of the ratio of CC- to NC-events, as with this quantity the  $\nu_e$ -contribution to the total solar neutrino flux is connected. A measured CC/NC-ratio smaller than the standard one unambiguously proves that the solar neutrinos, initially  $\nu_e$ 's, are oscillating into another flavor during their flight from the solar interior to the Earth.

If the excess in the high-energy bins of Super-Kamiokande, which was apparent in the previous data published [14], reappears in the continuing measurements, the CC/NC-ratio in SNO will enable to discriminate between an explanation by neutrino oscillations and by an enhanced *hep*-neutrino flux, which also was under discussion [19]. While for the latter solution the *hep*-neutrinos would equally contribute to the CC- and NC-events leading to a constant CC/NC-ratio, for the oscillation scenario a similar excess like in Super-Kamiokande would be also apparent in the CC/NC-ratio of SNO.

To illustrate the expectations for the recoil-deuterium energy spectrum and zenith-angle dependence of the CC-events in SNO, the first and second moments of these distributions are calculated (for definition see [13]). The first moment provides the mean value and the second a measure of the width of the distribution.

With very small annual or daily changes in the Super-Kamiokande detector, such variations are neither expected for CC-events ( $e-\nu_e$ -scattering) in SNO. Thus, for the zenith-angle moments in SNO only small deviations from the standard value are predicted for the 2-flavor SMA-, LMA-, LOW-, and VO-solutions (Fig. 18(b)). The largest deviations of about 4% may be measured in case of the LMA-solution being correct.

The error bars for these solutions in Fig. 18 were obtained in the same manner as for the recoil-electron energy spectrum in Borexino. Since the best-fit values are not very well separated and also the error bars strongly overlap in the plane of the first two zenith-angle moments, it seems to be very difficult to disentangle the 2-flavor solution by forthcoming zenith-angle data of

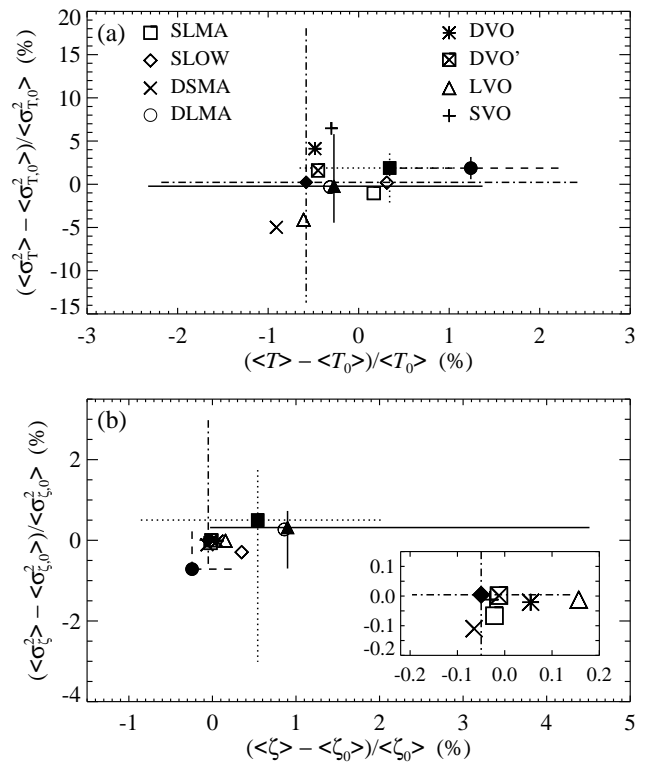


FIG. 18. Predicted values for the moments of the recoil-deuterium energy (upper panel) and zenith-angle spectrum (lower panel) for CC-events in SNO in case of the 3-flavor solutions. The filled symbols represent the 2-flavor solutions LMA ( $\blacktriangle$ ), SMA ( $\bullet$ ), LOW ( $\blacksquare$ ) and VO ( $\blacklozenge$ ) of Fig. 4. The error bars were obtained in the same manner as the hashed resp. shaded areas in Fig. 16.

SNO. A similar behavior is expected for the moments of the recoil-deuterium energy spectrum [53] shown in Fig. 18(a). However, since the energy resolution in SNO is better than in Super-Kamiokande (Table VI) more significant data can be expected to disentangle the true solution to the solar neutrino problem. A more detailed discussion about the properties of SNO to discriminate the 2-flavor solutions can be found in [54].

In the energy moments a large area is still allowed for the VO-solution. In case Borexino does not record any seasonal variations all solutions containing a VO-branch (e.g. LVO), and in particular the 2-flavor VO-solution would hardly be correct. Deviation of  $< -5\%$  in the second energy moment would then favor the DSMA-solution.

Nevertheless, from Fig. 18 it becomes obvious that, only if SNO is measuring a big deviation of the energy or zenith-angle moment from the standard (no-oscillation) value, one of these solution can be favored, as e.g.  $\gtrsim 3\%$  in the first zenith angle further supports LMA as correct solution to the solar neutrino problem. But, since SNO may well detect no such deviations, we need additional results from Borexino to exclude some of the presently

<sup>††</sup> Provided, no mixing with sterile neutrinos occurs.

possible solutions.

## VI. DISCUSSION

The most favored solutions to the solar neutrino problem in the scope of 2- and 3-flavor neutrino oscillations have been investigated in this work. For this purpose the evolution of the neutrino state was followed numerically from the solar interior, where the neutrinos are produced in the fusion reactions, through Sun, space and Earth to the neutrino detectors without falling back to analytical approximations (cf. Appendix).

Eight new solutions in the 3-flavor case could be found, among which SVO, SLMA, and DSMA are at least as probable as the presently favored 2-flavor LMA-solution. The DVO-, DVO', LVO, DLMA-, and, SLOW-solutions, with which the measured event rates, recoil-electron energy spectrum, zenith-angle dependence and annual variation are reproduced slightly worse than with the other three 3-flavor solutions, are nevertheless still good candidates as solution to the solar neutrino problem. The new experiments Borexino and SNO, which recently have started to operate, and improved statistics in Super-Kamiokande possibly will possibly enable to discriminate the various 2- and 3-flavor solutions. Basically, with Borexino the vacuum-oscillation solutions will leave a clear footprint in the annual variation of the event rates, with which they can be distinguished from MSW-solutions. Additionally, in case of the SLOW-solutions the high energy bins of the recoil-electron energy spectrum will be significantly depleted compared to the other energy bins and a day-night asymmetry of about 10% is expected, which only can be reproduced by the 2-flavor LOW-solution.

In this work it was investigated whether the 2-flavor solutions of the solar neutrino problem can be improved by including all three flavors. But the 3-flavor case cannot be examined totally independent of the results obtained for the atmospheric neutrinos. The most promising solution to the atmospheric neutrino problem is presently the oscillation between  $\nu_\mu$  and  $\nu_\tau$  with the mass-squared difference  $\Delta m_{23}^2$  being approximately  $10^{-3} \text{ eV}^2$  [55]. This demands that the sum or difference of  $\Delta m_{12}^2$  and  $\Delta m_{13}^2$  of the 3-flavor solutions for the solar neutrino problem is about  $10^{-3} \text{ eV}^2$ . However, none of the presented 3-flavor solutions fulfills this condition, which implies that either 3-flavor solutions are excluded favoring the 2-flavor LMA-solution ( $\Theta_{13} = 0$ ) or that the origin of the atmospheric neutrino problem are not  $\nu_\mu$ - $\nu_\tau$ -oscillations.

But analyzing the atmospheric neutrino deficit using 3-flavor neutrino oscillations it has been found that with  $\Delta m_{23}^2 \approx 10^{-4} \text{ eV}^2$  solutions exist, if  $\Delta m_{12}^2$  and  $\sin^2 2\Theta_{12}$  are in the vicinity of the SMA-solution and  $4^\circ \lesssim \Theta_{13} \lesssim 22^\circ$  (Fig. 2(d) in [56]). Indeed, the SLMA-solution fulfills this condition as its SMA-branch ( $\nu_1 \leftrightarrow \nu_2$ ) is close to the 2-flavor SMA-solution and the best-fit parameters of

the LMA-branch are  $\Delta m_{13}^2 = 2.5 \times 10^{-4}$  and  $\Theta_{13} = 19^\circ$  (cf. Table V). This solution is close to the best 3-flavor solution found recently in [21], where the 825-days data of Super-Kamiokande have been employed and where a priori  $\Delta m_{13}^2 \gg 10^{-4} \text{ eV}^2$  has been assumed. The solution in [21] represents not the optimal fit to the data in the vicinity of the SLMA-solution, as with the best-fit value for  $\Delta m_{13}^2$  being  $2.5 \times 10^{-4} \text{ eV}^2$  certainly the conditions assumed therein are not fulfilled. Therefore, a fully consistent 3-flavor analysis of the solar and atmospheric neutrino data should be performed to find the most probable mixing parameters of the neutrinos.

An additional candidate, which appears to be consistent with the atmospheric neutrino results, is the LVO-solution, the LMA-branch of which ( $\nu_1 \leftrightarrow \nu_3$ ) has similar parameters as the SLMA-solution (Table V). However, since the oscillation length of the VO-branch in LVO is much larger than the Earth diameter,  $\nu_1 \leftrightarrow \nu_2$ -oscillations have no effect on atmospheric neutrinos. Hence, the pure 2-flavor analysis can be performed for the atmospheric neutrino oscillations favoring  $\Delta m_{23}^2 = \Delta m_{13}^2 \approx 10^{-3} \text{ eV}^2$ .

A further possible solution to the atmospheric neutrino problem may be the oscillation into a sterile neutrino, which is neglected in this work. So, it cannot be excluded that 3-flavor oscillation solutions with a sterile and an active neutrino-branch exist, which solve the solar and atmospheric neutrino problem, too.

In the 2-flavor solutions LMA, SMA, LOW, and VO it is implicitly assumed that the mixing into the third flavor is negligible. Thus, these solutions are not coupled to the atmospheric neutrino problem, as they can easily be taken as  $\nu_e$ - $\nu_\mu$ -oscillations, where no mixing between  $\nu_e$  and  $\nu_\tau$  appears. If however the results of the LSND-collaboration [57], which claimed to have detected  $\nu_e$ - $\nu_\mu$ -oscillations with  $\Delta m_{12}^2 \gtrsim 10^{-2} \text{ eV}^2$ , are confirmed by KARMEN2 [58], it will be difficult to solve the solar and atmospheric neutrino anomaly simultaneously by the oscillation of three neutrino flavors. A 4-neutrino scheme has been proposed (one sterile and three active neutrinos) to cover the three different mass scales involved by the LSND-result, atmospheric and solar neutrino problems [59]. In any case, identifying the solution to the solar neutrino puzzle by future data of forthcoming and presently operating solar-neutrino detectors may also constrain the solutions for the atmospheric neutrino problem or vice versa.

The possibility that 2-flavor neutrino oscillations are responsible for the solar neutrino puzzle appears to be supported by the relatively weak improvement of the fit by increasing the parameter space from 2 (two flavors) to 4 dimensions (three flavors). Indeed, only with the SVO-solution a somewhat better fit to the data could be achieved compared to the LMA-solution. This can be taken as a hint, that the errors in the data of Super-Kamiokande are greater than assumed, perhaps still unknown systematic errors are apparent, or that the statistics is still insufficient. Moreover, correlations between the different data sets of Super-Kamiokande probably are

important for a more accurate and reliable analysis of the solar neutrino data.

Anyway, if the explanation of the atmospheric neutrino deficit is, despite the presently strong evidence, found not to be neutrino oscillations, 3-flavor oscillations are allowed in any mass range, implying that the SVO-solution leads to the best fit to the data. Remarkably, SVO has been found to be the favored solution also when taking the previous 504- or 708-days data sets of Super-Kamiokande [9]. Hence, SVO is together with the 2-flavor LMA-solution one of the stablest explanation for the solar neutrino problem.

## ACKNOWLEDGMENTS

I am grateful to Achim Weiss and Wolfgang Hillebrandt for their inspiring comments and suggestions. Furthermore, the support of Georg Raffelt in particle-physics questions is acknowledged. I also want to thank Jørgen Christensen-Dalsgaard for his help in further improving the solar model. Moreover, I am thankful to Sarbani Basu for providing me the seismic model, to Scilla Degl'Innocenti for the seismic error data, to John N. Bahcall for the detector response functions and other useful quantities of SNO and to Lothar Oberauer for the data about the Borexino properties. This work was supported by the ‘‘Sonderforschungsbereich 375-95 für Astroteilchenphysik’’ der Deutschen Forschungsgemeinschaft.

## APPENDIX: FROM THE INITIAL NEUTRINO STATE TO THE EVENT RATES

To obtain event rates for the various detectors a variety of averages and integrals have to be evaluated. In this section briefly a numerical scheme is described, how accurate predictions for the event rates can be calculated numerically.

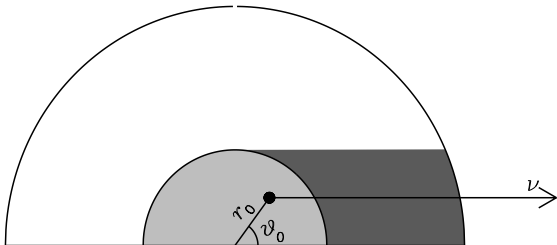


FIG. 19. Illustrating the definition of  $r_0$  and  $\vartheta_0$ . The light shaded region reflects the region of neutrino production, the dark shaded is covered by about 50 different paths (see text) with direction to the Earth (arrow labeled  $\nu$ ).

For a certain set of parameters  $\Delta m_{12}^2$ ,  $\Delta m_{13}^2$ ,  $\sin^2 2\Theta_{12}$ , and  $\sin^2 2\Theta_{13}$  the evolution of an initially pure electron-neutrino from the solar interior to the terrestrial detectors has to be evaluated. Therefore,

$$|\nu_i(r)\rangle = e^{-i\tilde{H}r}|\nu_i^e\rangle \quad (\text{A1})$$

must be integrated (cf. Eq. 5).  $|\nu_i^e\rangle$  denotes the initial electron-neutrino state given by Eq. (8). The evolution starts at a point inside the Sun given by  $r_0$  and  $\vartheta_0$  (see Fig. 19). The neutrino path has then to be followed through Sun, space and, if necessary, Earth arriving at the detector at the day  $D$  under the zenith angle  $\zeta$ . From the final state  $|\nu_i^f\rangle$  the electron-neutrino survival probability  $P_{e\rightarrow e}(\Delta m_{12}^2/E, \Delta m_{13}^2/E, \sin^2 2\Theta_{12}, \sin^2 2\Theta_{13}, r_0, \vartheta_0, D, \zeta)$  is derived using the relation

$$P_{e\rightarrow e} = |\langle \nu_i^f | \nu_i^e \rangle|^2. \quad (\text{A2})$$

Since none of the detectors is able to discriminate between  $\nu_\mu$  and  $\nu_\tau$ , the contribution of these neutrino families is simply given by  $1 - P_{e\rightarrow e}$ .

First, the neutrino paths through the Sun are considered. Since  $N_e$ , and thus also the Hamiltonian  $\tilde{H}$ , is a function of  $r$  the integration of Eq. (A1) is performed piecewise. For this purpose, the interior of a solar model is subdivided into a grid equally spaced in electron density (about 500 grid points). By approximating the electron density between two neighboring grid point linearly, Eq. (A1) can be solved analytically. Thereby the neutrino state can be followed through the whole solar interior. Furthermore, the accuracy is improved by increasing the grid density near the resonance (Eq. 11).

Most of the neutrinos emerge between  $0 < r_0 \lesssim 0.4R_\odot$  and  $0 \leq \vartheta_0 \leq \pi$ . If the MSW-resonance lies within this region, it is crucial to carefully calculate the paths for neutrinos with different  $r_0$ , as the more centrally produced neutrinos may undergo a MSW-conversion, while the outermost are hardly influenced by the matter. Paths with  $\vartheta_0 > \pi/2$  may even twice cross the MSW-resonance region. The contribution of a neutrino emerging at an angle  $\vartheta_0$  and radius  $r_0$  to the total flux originating in this shell is given by

$$\Omega(\vartheta_0) = 0.5 \sin(2\vartheta_0) d\vartheta_0$$

for  $0 \leq \vartheta_0 \leq \pi/2$ . From the symmetry around the plane  $\vartheta_0 = \pi/2$  it follows that  $\Omega(\vartheta_0) = \Omega(\pi - \vartheta_0)$ .

Since all neutrinos cross the shell  $0.4R_\odot \lesssim r_0 \leq R_\odot$  a set of paths through this area is established (generally about 50 equally spaced in  $\sin \vartheta_0$ ) on which  $\exp(-i\tilde{H}r)$  is calculated numerically by adding up the solutions in each region linearized in  $N_e$ . Thus, a set of matrices is obtained  $\mathcal{S}_\odot(\sin \vartheta_0)$  which describes the evolution from  $r \approx 0.4R_\odot$  to the solar surface. By this means the neutrino state  $|\nu_i^\odot(r_0, \vartheta_0)\rangle$  is evaluated by first integrating Eq. (A1) until  $r \approx 0.4R_\odot$  and then using that matrix

$\mathcal{S}_\odot(\sin\vartheta_0)$ , which was calculated for a path closest to the actual path of  $|\nu_i(r_0, \vartheta_0)\rangle$ . It turns out that calculating solely two paths ( $\vartheta_0 = 0$  and  $\pi$ ) yields mostly already acceptable results. In this case, of course, only one matrix  $\mathcal{S}_\odot(0)$  is needed.

Now, the state  $|\nu_i^\odot(r_0, \vartheta_0)\rangle$  is followed until the surface of the Earth using the equation for the vacuum oscillations (Eq. 6). Since the Earth orbit is eccentric, different days  $D$  during a year are discriminated (about 20 from perihelion to aphelion). In a final step the rotation of the Earth and thus the different paths of a neutrino through the Earth's interior during one day are considered. Here a procedure similar to the shell outside the fusion region of the Sun is applied: A set of about 30 matrices  $\mathcal{S}_E(\sin\zeta)$  is calculated integrating  $\exp(-i\tilde{H}r)$  through the Earth.

By applying finally Eq. (A2) the survival probability  $P_{e\rightarrow e}(r_0, \vartheta_0, D, \zeta)$  for a certain set of parameters  $\Delta m_{12}^2/E$ ,  $\Delta m_{13}^2/E$ ,  $\sin^2 2\Theta_{12}$ ,  $\sin^2 2\Theta_{13}$  is obtained. This is the basic quantity from which the final event rates are calculated.

Since the experiments provide data binned in certain periods (e.g. day, night, annual seasons or a whole year) resp. in certain ranges of the zenith angle,  $P_{e\rightarrow e}(r_0, \vartheta_0, D, h)$  first has to be integrated using the zenith-angle weights  $W_\lambda(\zeta, D)$  (see e.g. [13]) for each period  $D$  at the detector latitude  $\lambda$ .

After that,  $P_\lambda^k(r_0, \vartheta_0)$  is folded with the radial distribution  $\Phi_r(r_0)$  of the neutrino sources inside the Sun and the angle weights  $\Omega$  discriminating the different neutrino types ( $pp$ ,  ${}^7\text{Be}$ ,  ${}^8\text{B}$  etc., denoted by the superscript  $f$ ). The event rates in the detectors are obtained by finally folding  $P_\lambda^f$  with the energy spectrum of each neutrino type  $\Phi_E^f$  and the detector response function  $\Xi_i(E)$ , and summing up the contribution of all neutrino types. This yields

$$N_i = \sum_f \int P_\lambda^f \Xi_i(E') \Phi_E^f(E') dE', \quad (\text{A3})$$

where  $i$  is either Ga or Cl. The detector response function for the Homestake detector can be found e.g. in [18] and for the Ga-detectors in [60].

In Super-Kamiokande, Borexino and SNO the energy spectrum of the recoil electrons (resp. deuterium atoms) can be measured at least within certain energy bins. Furthermore, SNO is able to discriminate CC- and NC-events, while Super-Kamiokande and Borexino measure the total number of events arisen by any neutrino flavor. According to [53] the response function for these type of experiments with the recoil-electron energy between  $T_0$  and  $T_1$  can be described by

$$\Xi_\Upsilon(E, T_0, T_1) = \int_{T_0}^{T_1} dT \int dT' R(T, T') \frac{d\sigma_\Upsilon(E, T')}{dT'}, \quad (\text{A4})$$

where with

$$R(T, T') = \frac{1}{\sqrt{2\pi}\Delta_T} \exp\left(-\frac{(T' - T + \delta)^2}{2\Delta_T^2}\right)$$

the energy resolution of the detector is included. Therein  $\delta$  accounts for a possible uncertainty in the absolute energy calibration and  $\Delta_T$  is the energy resolution width following the photon statistics which yields

$$\Delta_T = \Delta_{10} \sqrt{\frac{T}{10 \text{ MeV}}}$$

with  $\Delta_{10}$  being the energy resolution at 10 MeV. The parameters  $\Delta_{10}$  and  $\delta$  for Super-Kamiokande, SNO and Borexino are summarized in Table VI.

TABLE VI. Energy resolution parameters used in the present work. The values for Super-Kamiokande and SNO are taken from [53]. For Borexino  $\Delta_1$  the energy resolution width at 1 MeV provided by L. Oberauer (private communication) is quoted.

	Super-K	SNO	Borexino
$\Delta_{10}$	1.6 MeV	1.1 MeV	47 keV
$\delta$	10 keV	100 keV	—

The cross sections  $\frac{d\sigma_\Upsilon(E, T)}{dT}$  for Super-Kamiokande and Borexino were calculated following the description in [61].  $\Upsilon$  denotes either  $\nu_e$  and  $\nu_\mu$  (or equivalent  $\nu_\tau$ ) for the interaction of these neutrino flavors with Super-Kamiokande and Borexino or CC resp. NC for the reaction type in the SNO detector. With  $\Xi_\Upsilon(E, T_0, T_1)$  given by Eq. (A4) the event rates in Borexino resp. Super-Kamiokande are obtained from

$$N_i^k(T_0, T_1) = \sum_f \int \left[ (1 - P_\lambda^{k,f}) \Xi_{\nu_\mu}(E', T_0, T_1) + P_\lambda^{k,f} \Xi_{\nu_e}(E', T_0, T_1) \right] \Phi_E^f(E') dE', \quad (\text{A5})$$

while the number of CC- and NC-events in SNO is defined analogous to the Gallium and Chlorine detector (Eq. A3). With the threshold energy being greater than 5 MeV only the sum over  ${}^8\text{B}$ - and  $hep$ -neutrinos has to be performed in Super-Kamiokande and SNO.

- 
- [1] R. Davis Jr., D. S. Harmer, and K. C. Hoffman, Phys. Rev. Lett. **20**, 1205 (1968).
  - [2] W. A. Dziembowski, P. R. Goode, A. A. Pamyatnykh, and R. Sienkiewicz, Astrophys. J. **445**, 509 (1994); S. Basu *et al.*, *ibid.* **460**, 1064 (1996); H. M. Antia, Astron. Astrophys. **307**, 609 (1996); S. Basu, M. H. Pinsonneault, and J. N. Bahcall, Astrophys. J. **529**, 1084 (2000).

- [3] H. Schlattl, A. Weiss, and H.-G. Ludwig, *Astron. Astrophys.* **322**, 646 (1997).
- [4] J. N. Bahcall, S. Basu, and M. H. Pinsonneault, *Phys. Lett. B* **433**, 1 (1998).
- [5] M. Gabriel, *Astron. Astrophys.* **309**, 939 (1996); O. Richard, S. Vauclair, C. Charbonnel, and W. A. Dziembowski, *ibid.* **312**, 1000 (1996).
- [6] P. Anselmann *et al.* (the GALLEX collaboration), *Phys. Lett. B* **285**, 376 (1992); the GALLEX-collaboration measured solar neutrinos from May 1991 to January 1998 interrupted by some maintenance work and calibration experiments. In July 1998 the facilities were taken over by the newly formed GNO-group (Gallium Neutrino Observatory). After an extension of the Gallium-target to 60 t and further technical improvements the detector has been taking data again since the spring of 1999.
- [7] J. N. Abdurashitov *et al.* (the SAGE collaboration), *Phys. Lett. B* **328**, 234 (1994).
- [8] N. Hata and P. Langacker, *Phys. Rev. D* **52**, 420 (1995).
- [9] H. Schlattl, Ph.D. thesis, Technical University Munich, 1999.
- [10] B. Pontecorvo, *Zh. Eksp. Teor. Fiz.* **53**, 1717 (1967) [*Sov. Phys. JETP* **26**, 984 (1968)].
- [11] S. P. Mikheyev and A. Yu. Smirnov, *Yad. Fiz.* **42**, 1441 (1985) [*Sov. Jour. Nucl. Phys.* **42**, 913 (1985)]; L. Wolfenstein, *Phys. Rev. D* **17**, 2369 (1978).
- [12] N. Hata and P. Langacker, *Phys. Rev. D* **56**, 6107 (1997); H. Schlattl, A. Bonanno, and L. Paternò, *ibid.* **60**, 113002 (1999); J. N. Bahcall, P. I. Krastev, and A. Yu. Smirnov, *Phys. Lett. B* **477**, 401 (2000).
- [13] J. N. Bahcall and P. I. Krastev, *Phys. Rev. C* **56**, 2839 (1997).
- [14] Y. Fukuda *et al.* (the Super-Kamiokande collaboration), *Phys. Rev. Lett.* **82**, 2430 (1999).
- [15] Y. Fukuda *et al.* (the Super-Kamiokande collaboration), *Phys. Rev. Lett.* **82**, 1810 (1999).
- [16] J. N. Bahcall, P. I. Krastev, and A. Yu. Smirnov, *Phys. Rev. D* **58**, 096016 (1998).
- [17] C. E. Ortiz *et al.*, *Phys. Rev. Lett.* **85**, 2909 (2000).
- [18] J. N. Bahcall *et al.*, *Phys. Rev. C* **54**, 411 (1996).
- [19] J. N. Bahcall, P. I. Krastev, and A. Yu. Smirnov, *Phys. Rev. D* **60**, 093001 (1999).
- [20] G. L. Fogli, E. Lisi, and D. Montanino, *Phys. Rev. D* **54**, 2048 (1996).
- [21] G. L. Fogli, E. Lisi, D. Montanino, and A. Palazzo, *Phys. Rev. D* **62**, 013002 (2000);
- [22] T. Teshima, T. Sakai, and O. Inagaki, *Int. J. Mod. Phys. A* **14**, 1953 (1999); J. S. Kim and C. W. Kim, hep-ph/9909428 (1999).
- [23] G. G. Raffelt, *Stars as Laboratories for Fundamental Physics* (University of Chicago Press, Chicago, 1996).
- [24] S. T. Petcov, *Phys. Lett. B* **214**, 259 (1988).
- [25] K. Dick, M. Freund, M. Lindner, and A. Romanino, *Nucl. Phys. A* **562**, 29 (1999).
- [26] V. Barger, K. Whisnant, S. Pakvasa, and R. J. N. Phillips, *Phys. Rev. D* **22**, 2718 (1980).
- [27] T. Ohlsson and H. Snellman, *J. Math. Phys.* **41**, 2768 (2000).
- [28] J. Lundell and H. Snellman, *Phys. Lett. B* **470**, 163 (1999).
- [29] A. Friedland, *Phys. Rev. Lett.* **85**, 936 (2000).
- [30] A. de Gouvêa, A. Friedland, and H. Murayama, *Phys. Lett. B* **490**, 125 (2000).
- [31] C. Caso *et al.* (Particle Data Group), *Eur. Phys. J. C* **3**, 1 (1998).
- [32] M. C. Gonzalez-Garcia and C. Peña-Garay, *Phys. Rev. D* **62**, 031301 (2000).
- [33] J. Bouchez *et al.*, *Z. Phys. C* **32**, 499 (1986); S. P. Mikheyev and A. Yu. Smirnov, in *Proceedings of the 7th Moriond Workshop on New and Exotic Phenomena*, edited by O. Fackler and T. T. Ván (Frontières, Paris, 1987), p. 405; M. Spiro and D. Vignaud, *Phys. Lett. B* **242**, 279 (1990).
- [34] T. K. Kuo and J. Pantaleone, *Phys. Rev. Lett.* **57**, 1805 (1986).
- [35] H. Schlattl and A. Weiss, *Astron. Astrophys.* **347**, 272 (1999).
- [36] F. J. Rogers, F. J. Swenson, and C. A. Iglesias, *Astrophys. J.* **456**, 902 (1996).
- [37] C. A. Iglesias and F. J. Rogers, *Astrophys. J.* **464**, 943 (1996).
- [38] E. G. Adelberger *et al.*, *Rev. Mod. Phys.* **70**, 1265 (1998).
- [39] A. A. Thoul, J. N. Bahcall, and A. Loeb, *Astrophys. J.* **421**, 828 (1994).
- [40] B. Freytag, H.-G. Ludwig, and M. Steffen, *Astron. Astrophys.* **313**, 497 (1996).
- [41] M. Canuto and I. Mazzitelli, *Astrophys. J.* **370**, 295 (1991); **389**, 724 (1992).
- [42] W. Hampel *et al.* (the GALLEX collaboration), *Phys. Lett. B* **447**, 127 (1999); M. Altmann *et al.* (the GNO collaboration), *ibid.* **490**, 16 (2000); J. N. Abdurashitov *et al.* (the SAGE collaboration), *Phys. Rev. C* **60**, 055801 (1999); G. Gavrin (for the SAGE collaboration), talk given at the XIX International Conference on Neutrino Physics and Astrophysics, Sudbury, Canada, June 2000.
- [43] B. T. Cleveland *et al.*, *Astrophys. J.* **496**, 505 (1998).
- [44] Y. Suzuki, talk given at the XIX International Conference on Neutrino Physics and Astrophysics, Sudbury, Canada, June 2000.
- [45] S. Basu, *Mon. Not. R. Astron. Soc.* **298**, 719 (1998).
- [46] J. Christensen-Dalsgaard *et al.*, *Science* **272**, 1286 (1996).
- [47] S. Degl'Innocenti, S. Dziembowski, W. A. Fiorentini, and B. Ricci, *Astropart. Phys.* **7**, 77 (1997).
- [48] A. M. Dziemowski and D. L. Anderson, *Phys. Earth Planet. Interior* **25**, 207 (1981).
- [49] V. Berezinsky, G. Fiorentini, and M. Lissia, *Astropart. Phys.* **12**, 299 (2000).
- [50] Q. Y. Liu and S. T. Petcov, *Phys. Rev. D* **56**, 7392 (1997).
- [51] K. S. Babu, Q. Y. Liu, and A. Yu. Smirnov, *Phys. Rev. D* **57**, 5825 (1998).
- [52] A. de Gouvêa, A. Friedland, and H. Murayama, *Phys. Rev. D* **60**, 093011 (1999).
- [53] J. N. Bahcall, P. I. Krastev, and E. Lisi, *Phys. Rev. C* **55**, 494 (1997).
- [54] J. N. Bahcall, P. I. Krastev, and A. Yu. Smirnov, *Phys. Rev. D* **62**, 093004 (2000).
- [55] Y. Fukuda *et al.* (the Super-Kamiokande Collaboration),

- Phys. Rev. Lett. **82**, 2644 (1999).
- [56] T. Sakai and T. Teshima, Prog. Theor. Phys. **102** 629 (1999).
- [57] C. Athanassopoulos *et al.* (the LSND Collaboration), Phys. Rev. C **58**, 2489 (1998).
- [58] K. Eitel, in *Lake Louise Winter Institute 1999* (Lake Louise, 1999), for the KARMEN Collaboration.
- [59] J. W. F. Valle, in *Corfu Summer Institute on Elementary Particle Physics, Kerkyra, Greece, 6-20 Sep 1998*, edited by I. Antoniadis, G. Koutsoumbas, N. Tracas, and G. Zoupanos (JHEP, 1998).
- [60] J. N. Bahcall, Phys. Rev. C **56**, 3391 (1997).
- [61] J. N. Bahcall, M. Kamionkowski, and A. Sirlin, Phys. Rev. D **51**, 6146 (1995).